# SODIUM MRI FOR STUDYING ISCHEMIC TISSUE IN ACUTE STROKE

by

**George Charles LaVerde**

BS, Duke University, 2000

Submitted to the Graduate Faculty of the

School of Engineering in partial fulfillment

of the requirements for the degree of

Doctor of Philosophy

University of Pittsburgh

2006

UNIVERSITY OF PITTSBURGH

SCHOOL OF ENGINEERING

This dissertation was presented

by

George Charles LaVerde

It was defended on

July 14, 2006

and approved by

Harvey Borovetz, Ph.D., Professor, Department of Bioengineering

George D. Stetten, M.D., Ph.D., Associate Professor, Department of Bioengineering

Clayton A. Wiley, M.D., Ph.D., Professor, Department of Pathology

Dissertation Director: Fernando E. Boada, Ph.D., Associate Professor, Departments of Radiology and Bioengineering

**SODIUM MRI FOR STUDYING ISCHEMIC TISSUE IN ACUTE STROKE**

George Charles LaVerde, Ph.D.

University of Pittsburgh, 2006

This thesis presents sodium magnetic resonance (MR) as an *in vivo* means for non-invasively visualizing the changes in cell sodium ion homeostasis that occur in ischemic tissue during acute stroke. Single quantum sodium magnetic resonance imaging (MRI) was used to determine the time course of tissue sodium concentration (TSC) in a non-human primate model of reversible focal brain ischemia. In each animal, TSC increased slowly and linearly as a function of time after the onset of focal brain ischemia. Changes in the TSC accumulation were seen upon reperfusion. The results demonstrate that the increase in TSC in ischemic tissue is readily measurable using sodium MRI at clinical magnetic field strengths (3.0 T) in acceptable imaging times (5 minutes). The results also indicate that sodium MRI can estimate the ischemia onset time based on the slope of the TSC increase. This could have potential benefits for extending the use of thrombolytic therapy to stroke patients that are unsure when their symptoms began.

Many studies have hypothesized that the best means for the *in vivo* study of the changes in cell sodium ion homeostasis that occur during brain ischemia is to use imaging schemes that isolate the sodium MR signal from the intracellular compartment. This thesis investigates the contribution of the extracellular sodium pool to the brain's triple quantum (TQ) sodium MR signal in the rat using the thulium shift reagent, $TmDOTP^{5-}$. Within the signal to noise ratio (SNR) of the experiment, there was no evidence of any extracellular contribution to the brain's TQ sodium MR signal.

Finally, TQ sodium MR images in the *in vivo* non-human primate are presented for the first time. Moreover, these images were obtained in clinically acceptable 18 minute data acquisition times. TQ sodium MRI during non-human primate focal brain ischemia identified large changes in the ischemic region as early as 34 minutes after the onset of ischemia. The increase in the TQ sodium MRI signal intensity observed in the ischemic hemisphere is hypothesized to be due to an increase in the intracellular sodium concentration as a result of impaired ion homeostasis during evolving brain ischemia.

## TABLE OF CONTENTS

## LIST OF TABLES

## LIST OF FIGURES

## PREFACE

I express my deep gratitude to Dr. Fernando Boada for the excellent guidance and training that he has provided me throughout this entire journey. Dr. Boada, thanks for all that you have invested in me. I thank Dr. Harvey Borovetz, Dr. George Stetten, and Dr. Clayton Wiley for all of their time, help, and feedback as members of my dissertation committee. I would also like to thank Dr. Charles Jungreis, Dr. Edwin Nemoto, Dr. Costin Tanase, Dr. Stephen Jones, and Dr. Alexander Kharlamov for their collaborations on the non-human primate studies.

To my family, especially my wife, Tara, and my mother, Charlotte, thanks for all of your constant love, support, and encouragement. Finally, I dedicate this work to my father, Dr. Philip S. LaVerde, who devoted his life to medicine and died of cancer in April of 2004. Dad, thanks for always being an inspiration – I love you and I miss you.

# 1.0 INTRODUCTION

Tomography is the creation of "images of the internal organization of an object without physically cutting it open" [1]. Tomography is of the utmost importance in the field of medicine. The 1960's and 1970's were ground-breaking years for tomography when many advances were made in the development of both X-ray computed tomography (CT) and magnetic resonance imaging (MRI). Currently, several tomographic imaging modalities are medically available, including CT, MRI, positron emission tomography (PET), single photon emission computed tomography (SPECT), and ultrasound imaging [1].

MRI produces images of internal physical and chemical characteristics from externally measured nuclear magnetic resonance (NMR) signals [1]. The well-known NMR phenomenon on which MRI is based was independently described in 1946 by both Felix Bloch at Stanford and Edward Purcell at Harvard [2]. In 1972, Paul Lauterbur, University of Pittsburgh alumnus and 2003 Nobel Laureate in medicine, developed the spatial information encoding principles, originally called zeugmatography, that made image formation using NMR signals possible [3]. The name of this new "nuclear magnetic resonance imaging" (NMRI) was later shortened to just "magnetic resonance imaging" (MRI) because of the negative connotations associated with the word "nuclear" [4].

The combination of MRI's many notable features sets it apart from other tomographic imaging modalities. First, with no mechanical adjustment to the imaging machinery, MRI can

generate two-dimensional image slices at any orientation, three-dimensional volumetric images, and even four-dimensional spatial-spectral distribution images. Second, unlike CT, which uses X-ray transmission, and PET and SPECT, which require the injection of radioactive isotopes for signal generation, MRI does not involve the use of harmful ionizing radiation. The radiofrequencies used in MRI are from a lower energy region of the electromagnetic spectrum than even visible light, infrared, and microwaves. Third, the different types of images that can be obtained from the same anatomical slice simply by using different data acquisition protocols make MRI truly a remarkable imaging modality [1].

## 1.1 NUCLEAR SPIN AND THE NUCLEAR MAGNETIC RESONANCE (NMR) PHENOMENON

Nuclei of atoms that have unpaired protons, unpaired neutrons, or both have a non-zero net nuclear spin and angular momentum, and therefore, demonstrate the phenomenon of nuclear magnetic resonance [5]. This nuclear spin, more formally called the nuclear spin quantum number, $I$, has an associated angular momentum represented by the vector, $\mathbf{J}$, which describes the rotational motion of the nucleus and has a magnitude given by

$$\left|\mathbf{J}\right| = J = \hbar\sqrt{I(I+1)} \tag{1.1}$$

where $\hbar = \frac{h}{2\pi}$ and $h$ is Planck's constant (6.6 x $10^{-34}$ J-s). In the classical vector model, a nucleus with non-zero nuclear spin ($I \neq 0$), and thus, non-zero spin angular momentum ($\mathbf{J} \neq 0$) can be visualized as physically spinning about its axis the way the earth spins around its axis [6]. Like any spinning charged object, such a nucleus creates a magnetic field around it that is similar

to that created by a tiny bar magnet, and is represented by the nuclear magnetic dipole moment (or simply magnetic moment) vector, $\boldsymbol{\mu}$ [1]. In fact, a fundamental relationship of particle physics is that the spin angular momentum and magnetic moment vectors are colinear and proportional to each other; thus,

$$\boldsymbol{\mu} = \gamma \mathbf{J} \tag{1.2}$$

where the scalar constant of proportionality, $\gamma$, known as the gyromagnetic ratio is a physical property of the specific nucleus [7]. The physical constant $\gamma$ has units of radians/second/Tesla; however, gyromagnetic ratios are often given in terms of the related constant $\not\gamma = \frac{\gamma}{2\pi}$ which has units of Hertz/Tesla. The NMR properties of some biologically important nuclei are displayed in Table 1.1 (where most of the information is from Lufkin 1990 [5]).

**Table 1.1: NMR Properties of Selected Biologically Important Nuclei**

| Nucleus | Spin Quantum Number ($I$) | Natural Abundance (%) | Relative Sensitivity | Gyromagnetic Ratio $\not\gamma$ (MHz/T) |
|---|---|---|---|---|
| $^{1}$H | 1/2 | 99.98 | 1.00 | 42.58 |
| $^{13}$C | 1/2 | 1.11 | 0.016 | 10.71 |
| $^{23}$Na | 3/2 | 100 | 0.093 | 11.26 |
| $^{31}$P | 1/2 | 100 | 0.066 | 17.24 |

The magnitude of the magnetic moment vector $\boldsymbol{\mu}$ is given by an expression similar to Eq. (1.1) [1]:

$$|\boldsymbol{\mu}| = \mu = \gamma\hbar\sqrt{I(I+1)} \tag{1.3}$$

In body tissues, or any NMR sample for that matter, in the absence of an external magnetic field the magnetic moments of the nuclei are randomly oriented due to thermal random motion [8]. Therefore, in the absence of an external magnetic field there is a zero net macroscopic magnetization (or bulk magnetization), $\mathbf{M}$, which is the sum of all the microscopic magnetic moment vectors:

$$\mathbf{M} = \sum_n \boldsymbol{\mu}_n = 0 \quad \text{(in absence of external magnetic field).} \tag{1.4}$$

To obtain a macroscopic magnetization, $\mathbf{M}$, the microscopic magnetic moment vectors need to be aligned by placing the body tissue or sample in a large external magnetic field (i.e. in the MRI magnet) [2]. By convention, this large static external magnetic field is known as the main magnetic field (or the $B_0$ field) and it is assumed to be in the z-direction of the laboratory frame ($\mathbf{B_0} = B_0\hat{k}$, where $\hat{k}$ is the unit vector in the z-direction) [1]. Unlike objects the size of Newtonian bar magnets and compasses which may align exactly with the $B_0$ field, nuclei are extremely small and instead of exactly following the rules of classical Newtonian physics, they must follow the rules of quantum mechanics which limit their magnetic moment vectors to a discrete set of orientations or states [5]. In fact, for a nucleus with a non-zero spin ($I \neq 0$), the magnetic moment vector $\boldsymbol{\mu}$ can assume exactly $2I+1$ possible orientations with respect to the direction of the $B_0$ field. These $2I+1$ discrete orientations of $\boldsymbol{\mu}$ correspond to the following $2I+1$ values of the magnetic quantum number $m_I$ [1]:

$$m_I = -I, -I+1, ...., I \tag{1.5}$$

The hydrogen nucleus ($^1$H) which consists of one proton and no neutrons is an example of a spin-1/2 system. MRI of the $^1$H nucleus (i.e. "proton MRI") makes up the vast majority of all clinical MRI performed today [9]. For all spin-1/2 systems, $I = 1/2$ and the $2(1/2)+1 = 2$ possible orientations for the magnetic moment vector $\boldsymbol{\mu}$ correspond to $m_I = -1/2$ or +1/2. Given the value of $m_I$, the z-component of the magnetic moment vector $\boldsymbol{\mu}$ (i.e. the component in the direction of the $B_0$ field) is known for certain and is given by

$$\mu_z = \gamma m_I \hbar \tag{1.6}$$

The $m_I = +1/2$ nuclei are in the lower energy state or the ground state and are usually referred to as aligned "parallel" to the $B_0$ field. The $m_I = -1/2$ nuclei are in the higher energy state or the excited state and are usually referred to as aligned "antiparallel" to the $B_0$ field [5].

The $B_0$ field causes the magnetic moment $\boldsymbol{\mu}$ of each nucleus to experience a net external torque given by

$$\boldsymbol{\tau}_{net,ext} = \boldsymbol{\mu} \text{ x } \mathbf{B_0} \tag{1.7}$$

In addition, Newton's second law for rotation specifies that the net external torque acting on the nucleus must equal the rate of change of the angular momentum $\mathbf{J}$ of the nucleus [10]:

$$\boldsymbol{\tau}_{net,ext} = \frac{d\mathbf{J}}{dt} \tag{1.8}$$

Equating the right sides of Eq.'s (1.7) and (1.8), and substituting $\boldsymbol{\mu} = \gamma \mathbf{J}$ from Eq. (1.2) results in

$$\frac{d\mathbf{J}}{dt} = \boldsymbol{\mu} \text{ x } \mathbf{B_0} = \gamma \mathbf{J} \text{ x } \mathbf{B_0} \tag{1.9}$$

Because the change in the angular momentum $\frac{d\mathbf{J}}{dt}$ is perpendicular to the angular momentum $\mathbf{J}$, the axis of the spinning nucleus (and therefore, the magnetic moment $\boldsymbol{\mu}$) moves in the direction

of the torque (the direction of $\frac{d\mathbf{J}}{dt}$) and precesses about the direction of the $B_0$ field [10]. This precession of the spinning nucleus in the $B_0$ field is analogous to the wobbling of a toy top that spins about its axis, but also wobbles about the vertical due to the earth's gravitational field [11]. The frequency of this nuclear precession is proportional to and determined by the gyromagnetic ratio $\gamma$ and the strength of the $B_0$ field according to the Larmor equation [12]:

$$\omega_0 = \gamma B_0 \tag{1.10}$$

Thus, when the body tissue or sample is in the external $B_0$ field, each microscopic magnetic moment vector is in either the "parallel" or "antiparallel" orientation precessing around the z-axis at the Larmor frequency of $\omega_0 = \gamma B_0$. The microscopic magnetic moment vectors are evenly spaced around the circle of precession so that there is no net transverse magnetization (i.e. perpendicular to the $B_0$ field) [8]. The transverse plane (i.e. the xy-plane) is the plane which is "transverse" relative to the main longitudinal axis of the system (i.e. relative to the direction of the $B_0$ field along the z-axis). More magnetic moment vectors are in the "parallel" lower energy orientation than in the "antiparallel" orientation, so that the sum of all of these microscopic magnetic moment vectors precessing around the external $B_0$ field produces a net macroscopic magnetization in the z-direction with a strength of $M_0$ [5]:

$$\mathbf{M} = \sum_n \boldsymbol{\mu}_n = M_0 \hat{k} \tag{1.11}$$

For clarity, the macroscopic magnetization vector $\mathbf{M}$ is described as having a longitudinal component $M_z$ along the z-axis called the "longitudinal magnetization" (in this case $M_z = M_0$)

and a transverse component $M_{xy}$ in the xy-plane called the "transverse magnetization" (in this case $M_{xy} = 0$) [13].

## 1.2 RADIOFREQUENCY ($B_1$) FIELD AND RELAXATION

In order to produce the MR signal that can be detected and processed, the net magnetization vector needs to be "excited" or rotated away from the z-direction into the transverse plane where it will cause a signal in the radiofrequency receiver coils. This is achieved by applying a magnetic field rotating in the transverse plane at the exact same frequency at which the microscopic magnetic moment vectors are precessing (i.e. at the Larmor frequency, which is in the radiofrequency range of the electromagnetic spectrum). This rotating magnetic field, called the radiofrequency (RF) field or the $B_1$ field [5], is much weaker than the $B_0$ field and it is normally turned on for only a few hundred microseconds to milliseconds, therefore, it is often referred to as the RF pulse [1].

The rotating $B_1$ field causes a torque on the macroscopic magnetization $\mathbf{M}$ that acts to rotate it away from its equilibrium longitudinal position (along the z-direction of the $B_0$ field) down toward the transverse plane, while $\mathbf{M}$ continues to precess about the z-axis at the Larmor frequency [8]. In other words, the torque due to the rotating $B_1$ field causes $\mathbf{M}$ to be slowly deflected away from the z-axis down toward the xy-plane more and more during each precessional cycle about the z-axis. If the $B_1$ field or RF pulse is applied for a long enough period of time, the original longitudinal macroscopic magnetization $\mathbf{M} = M_0\hat{k}$ will be slowly rotated away from the z-axis enough that it lies completely in the transverse plane, 90° from

where it started. The RF energy required to achieve this is called a 90° pulse [8]. In fact, the amplitude and duration of the $B_1$ field determines the amount of the final tip of **M** away from the longitudinal z-axis toward the transverse plane, and this angle is referred to as the "tip" or "flip" angle [5].

Immediately following a 90° RF pulse, the magnetization **M** (still precessing about the z-axis) lies completely in the transverse plane ($M_{xy} = M_0$ and $M_z = 0$) [12]. This transverse magnetization precessing in the transverse plane induces an electrical signal in the radiofrequency receiver coils called a free induction decay (FID). However, according to the laws of thermodynamics, the magnetization will return to its longitudinal state along the z-axis in equilibrium with the $B_0$ field provided that sufficient time is given. This process of returning to its pre RF pulse equilibrium state is characterized by the destruction of the transverse magnetization $M_{xy}$, called transverse relaxation, and the recovery of the longitudinal magnetization $M_z$, called longitudinal relaxation [1].

The destruction of the transverse magnetization occurs exponentially according to the equation

$$M_{xy}(t) = M_0 e^{-t/T_2} \tag{1.12}$$

where $T_2$ is the transverse relaxation time constant. In an NMR experiment, the echo time (TE) represents the time after the RF excitation pulse at which the transverse magnetization signal is recorded (or "sampled" or "acquired") so that the signal loss due to the transverse relaxation $T_2$ is given by the factor $e^{-TE/T_2}$. The recovery of the longitudinal magnetization also occurs exponentially, but with a different time constant, according to the equation

$$M_z(t) = M_0\left(1 - e^{-t/T_1}\right) \tag{1.13}$$

where $T_1$ is the longitudinal relaxation time constant [9]. In a typical NMR experiment, the RF excitation pulse and the sampling of the transverse magnetization signal are repeated many times consecutively, and then averaged together to increase the signal-to-noise ratio (SNR). The repetition time (TR) is the time between successive RF excitation pulses. Therefore, at each subsequent RF excitation pulse, the longitudinal magnetization is only $M_z(t) = M_0\left(1 - e^{-TR/T_1}\right)$, and that is the amount of magnetization that is "flipped" down into the transverse plane for the next signal acquisition. Thus, the signal loss due to the longitudinal relaxation $T_1$ is given by the factor $\left(1 - e^{-TR/T_1}\right)$.

## 1.3 GRADIENT FIELDS AND K-SPACE ENCODING

If the nuclear spins within the body tissue or sample experience only the main magnetic field, $B_0$, and the radiofrequency excitation field, $B_1$, then the magnetic resonance signals from different locations within the sample are generally indistinguishable. Spatial information encoding is achieved in MRI through the use of gradient magnetic fields, $B_G$, in addition to the $B_1$ and $B_0$ fields. A gradient magnetic field is a purposely inhomogeneous magnetic field whose z-component varies depending on the position, $\mathbf{r} = (x, y, z)$, within the sample so that the Larmor frequency of precession of the nuclear spins becomes a function of position [1]. For example, if after an excitation the sample experiences the homogeneous $B_0$ field, $\mathbf{B_0} = B_0\hat{k}$, plus a gradient field, $\mathbf{B}_G(\mathbf{r}) = B_G(\mathbf{r})\hat{k}$, then the total magnetic field experienced is $\mathbf{B} = \left(B_0 + B_G(\mathbf{r})\right)\hat{k}$, and the Larmor frequency at position, $\mathbf{r}$, is:

$$\omega(\mathbf{r}) = \gamma\left(B_0 + B_G(\mathbf{r})\right) = \omega_0 + \gamma B_G(\mathbf{r}) \tag{1.14}$$

Typically the gradient magnetic field always varies linearly and the gradient field can be written as $\mathbf{B}_G(\mathbf{r}) = B_G(\mathbf{r})\hat{k} = \left(G_x x + G_y y + G_z z\right)\hat{k}$, where $G_x$ is called the x-gradient, $G_y$ is called the y-gradient, and $G_z$ is called the z-gradient. These three gradients are often grouped into a gradient vector, $\mathbf{G} = (G_x, G_y, G_z)$, so that the gradient magnetic field can be written as:

$$\mathbf{B}_G(\mathbf{r}) = B_G(\mathbf{r})\hat{k} = \left(G_x x + G_y y + G_z z\right)\hat{k} = \left(\mathbf{G}\bullet\mathbf{r}\right)\hat{k} \tag{1.15}$$

The gradient magnetic field is generally a function of time so that Equation (1.15) becomes:

$$\mathbf{B}_G(\mathbf{r},t) = B_G(\mathbf{r},t)\hat{k} = \left(G_x(t) x + G_y(t) y + G_z(t) z\right)\hat{k} = \left(\mathbf{G}(t)\bullet\mathbf{r}\right)\hat{k} \tag{1.16}$$

There turns out to be a very important connection between this spatial information encoding method and the Fourier transform which enables the description of complex imaging schemes using "k-space" notation [1]. This k-space notation defines a k-space vector, $\mathbf{k} = (k_x, k_y, k_z)$, as the integral over time of the gradient vector $\mathbf{G}(t)$:

$$\mathbf{k}(t) = \frac{\gamma}{2\pi}\int_0^t \mathbf{G}(\tau)d\tau \tag{1.17}$$

If the desired image is represented by a three-dimensional function, $f(x, y, z)$, where the position vector $\mathbf{r} = (x, y, z)$ within the image is in units of length (cm), then the k-space vector, $\mathbf{k} = (k_x, k_y, k_z)$, represents the Fourier transform space of the position vector and has units of inverse length (1/cm), also called spatial frequency. The amplitude and duration of the $G_x$, $G_y$, and $G_z$ gradients are varied in order to move in the $k_x$, $k_y$, and $k_z$ directions in k-space, respectively, and the MR signal in the RF receiver coils, $S(k_x, k_y, k_z)$, is acquired at these different points in k-space. The general imaging equation provides the relationship between the

acquired MR signal $S(k_x, k_y, k_z)$ and the desired image $f(x, y, z)$, and is in the form of a three-dimensional Fourier transform [1]:

$$S(k_x, k_y, k_z) = \int_{-\infty}^{\infty}\int_{-\infty}^{\infty}\int_{-\infty}^{\infty} f(x, y, z)e^{-i2\pi(k_x x + k_y y + k_z z)}dxdydz \tag{1.18}$$

Therefore, once all of three-dimensional k-space has been sampled, the desired image function $f(x, y, z)$ can be obtained by taking the three-dimensional inverse Fourier transform of the acquired MR signal $S(k_x, k_y, k_z)$.

## 1.4 SODIUM MRI

Magnetic resonance imaging of the sodium nucleus is aptly named "sodium MRI." The sodium nucleus, $^{23}$Na, which represents 100% of the natural abundance of sodium, provides the strongest non-proton (non-$^{1}$H) nuclear magnetic resonance (NMR) signal that can be detected in the human body [14]. As presented in Table 1.1, $^{23}$Na has a spin quantum number of $I = 3/2$. Therefore, the $^{23}$Na nucleus, which consists of eleven protons and twelve neutrons, is an example of a spin-3/2 system. As given by Equation (1.5) for a spin-3/2 system, the sodium nucleus has $2(3/2)+1 = 4$ possible orientations for the magnetic moment vector $\boldsymbol{\mu}$ with respect to the direction of the $B_0$ field, and these four possible orientations correspond to $m_I = -3/2,\ -1/2,\ +1/2,$ and $+3/2$, where $-3/2$ is the highest energy state and $+3/2$ is the lowest energy state. Thus, there are three possible single quantum (SQ) transitions: the $-1/2 \leftrightarrow +1/2$ transition is an "inner" transition, while the $-3/2 \leftrightarrow -1/2$ and $+1/2 \leftrightarrow +3/2$ transitions are "outer" transitions [15].

### 1.4.1 Single Quantum Sodium MRI

Following the typical single RF excitation pulse, the free induction decay (FID) from the sodium nuclei within the sample is the sum of the signals from the three SQ transitions, which is why this type of MR sequence is called "SQ" sodium MR [15]. Because the $^{23}$Na nucleus has a spin quantum number greater than or equal to one, it possesses a quadrupole moment, which then interacts with any fluctuating electric field gradients that are present. If these quadrupolar interactions average to zero, then the inner and outer transitions have the same transverse relaxation rate, and the resulting FID is the simple sum of all three SQ transitions. However, fluctuating electric field gradients with correlation times longer than the Larmor period cause quadrupolar interactions that do not average to zero, perturbing the four possible energy levels [16]. The outer transitions are more strongly affected by these non-zero quadrupolar interactions than the inner transition. The resulting FID is then a weighted sum of the signals from the three SQ transitions, where the two outer SQ transitions, which make up 60% of the signal, relax with a very fast transverse relaxation rate ($T_{2,fast}$), and the inner SQ transition, which makes up the other 40% of the signal, relaxes with a slightly slower transverse relaxation rate ($T_{2,slow}$) [16].

This fast, bi-exponential transverse relaxation decay is one of the key NMR properties of the sodium nucleus. In fact, it is one of the key reasons why the signal-to-noise ratio (SNR) has previously been inadequate for sodium MRI to be effective. Because tissue sodium has such a fast, bi-exponential transverse relaxation decay, the echo time (TE) is one of the most influential acquisition parameters on the image quality of sodium MRI, and the use of conventional $^{1}$H MRI spatial encoding schemes [17] leads to TE's that are too long for sodium MRI. In other words, because of sodium's fast $T_2$'s, long TE's result in poor SNR and poor sensitivity of the image

intensity to changes in the tissue sodium concentration [18]. Only recently have advances in MRI technology and scanning hardware, such as new k-space trajectory schemes, allowed short enough TE's in sodium MRI sequences to provide adequate increases in image SNR in order to allow sodium MRI to become a useful reality [18-23]. The introduction of the twisted projection imaging (TPI) technique developed in our lab by Boada et al. [19] has provided a fast acquisition scheme capable of ultra-short TE's.

This TPI approach has been implemented to perform all sodium MR imaging described in this dissertation. TPI achieves short TE's by not requiring the use of phase encoding gradients, and also by making all of the k-space trajectories begin at the center of k-space. TPI uses three dimensional, constant sample density, k-space trajectories that lie on the surface of concentric cones in k-space (each cone having its point at the center of k-space). Figure 1.1 shows a graphical representation of these TPI k-space trajectories. The k-space trajectories depart from the center of k-space along radial lines up to a distance $pK_{max}$ ($p$<1), where $K_{max}$ is the maximum distance to be traveled in k-space. At the distance $pK_{max}$, the trajectories turn and start spiraling around the surface of the cone, moving gradually away from the point of the cone at the center of k-space, while maintaining a constant sample density. These k-space trajectories can be shown to require a maximum gradient slew rate, $S$, of

$$S = \frac{\gamma G^2 L}{p} \tag{1.19}$$

where $\gamma$ is the gyromagnetic ratio, $G$ is the gradient strength, $L$ is the field of view, and $p$ is the fraction of $K_{max}$ to be traversed along the radial line.

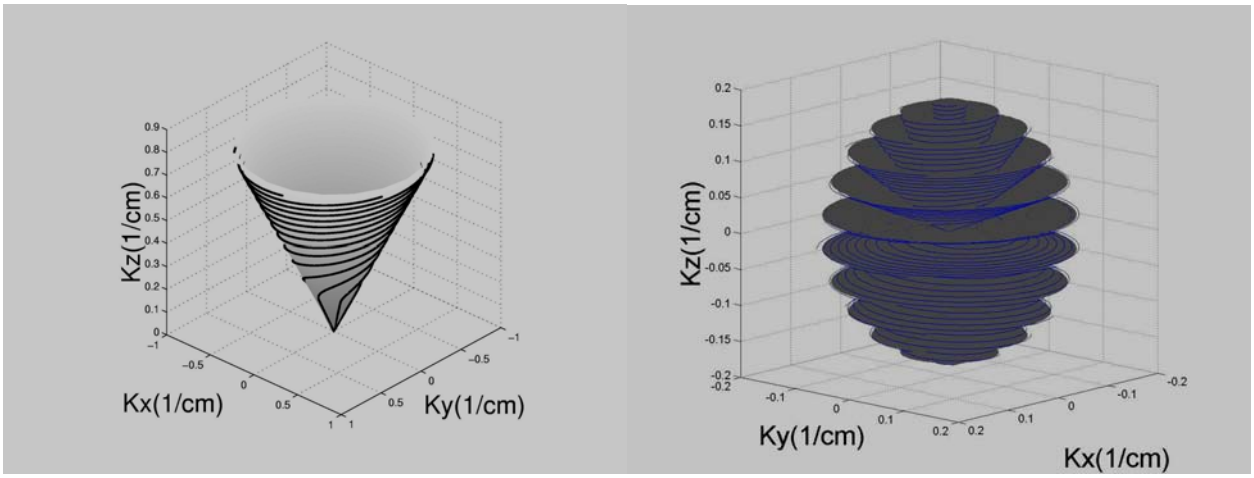


**Figure 1.1: Twisted Projection Imaging k-space Trajectories**

**Twisted projection imaging three dimensional, constant sample density, k-space trajectories on the surface of a single cone (left) and then on the surface of concentric cones in k-space (right) with each cone having its point at the center of k-space. All of the trajectories combined efficiently sample k-space in 3D.**

Using TPI, the conversion of the SQ sodium MRI signal to tissue sodium concentration (TSC) is commonly achieved by placing sodium calibration standards of known sodium concentrations within the image field of view (FOV) [18, 20-22]. Consequently, SQ sodium MRI using TPI can provide a non-invasive method for the *in vivo* measurement of TSC.

### 1.4.2 Triple Quantum Sodium MRI

Unlike the $^{1}H$ nucleus, the $^{23}Na$ nucleus with its four possible energy levels can experience multiple quantum (MQ) transitions in addition to the usual SQ transitions. For MQ transitions to be possible, the inner and outer transitions must have two different transverse relaxation rates [15, 16, 24, 25]. As discussed previously, this occurs when there are fluctuating electric field gradients with correlation times longer than the Larmor period, which cause quadrupolar

interactions that do not average to zero. In addition to the criteria of having non-zero quadrupolar interactions that cause the inner and outer transitions to have different transverse relaxation rates, a minimum of three RF pulses are necessary to produce detectable MQ sodium MR signal [15, 16, 24, 25]. For example, all triple quantum (TQ) sodium MR performed in this thesis implemented the three-pulse triple quantum coherence transfer filter presented by Hancu et al. [16] (shown in Figure 1.2), in which the first RF pulse creates SQ coherences, the second RF pulse transfers these SQ coherences to the TQ transition of the $^{23}$Na spin system (–3/2 ↔ +3/2), and the last RF pulse transforms these TQ coherences into detectable transverse magnetization. In this TQ pulse sequence shown in Figure 1.2, $\theta$ is the flip angle which is the same for all three pulses, $\phi_1$, $\phi_2$, and $\phi_3$ are the phases of the RF pulses, $\tau_1$ is the preparation time which allows the creation of the TQ coherences, and $\tau_2$ is the evolution time which allows their propagation.

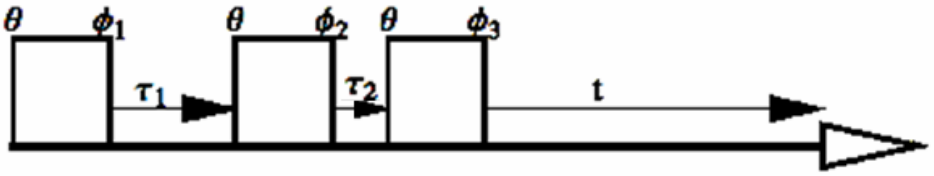


**Figure 1.2: Three-Pulse Triple Quantum Coherence Transfer Filter for TQ Sodium MR**
**The three-pulse triple quantum coherence transfer filter pulse sequence used for all TQ sodium MR performed in this thesis, in which the flip angle $\theta$ is the same for all three pulses, $\phi_1$, $\phi_2$, and $\phi_3$ are the phases of the RF pulses, $\tau_1$ is the preparation time which allows the creation of the TQ coherences, and $\tau_2$ is the evolution time which allows their propagation.**

The intensity of the TQ sodium MR signal depends on how different the fast and slow transverse relaxation rates are:

$$I = A\left(\exp\left(-\tau_1 / T_{2,\,fast}\right) - \exp\left(-\tau_1 / T_{2,slow}\right)\right)\exp\left(-\tau_2 / T_{2,slow}\right) \tag{1.20}$$

where $T_{2,\,fast}$ is the fast transverse relaxation rate, $T_{2,slow}$ is the slow transverse relaxation rate, A is a constant depending on the number of nuclei producing the signal and the line shape, $\tau_1$ is the pulse sequence preparation time, and $\tau_2$ is the pulse sequence evolution time. Equation (1.20) demonstrates that the TQ sodium MR signal is zero if the transverse relaxation rates for the inner and outer transitions are equal.

Several reports have demonstrated that the MQ sodium NMR signal from biological tissue comes primarily from the sodium in the intracellular space [14, 15, 25-29, 30] as opposed to the total tissue sodium content as measured in total (SQ) sodium MRI. This feature of MQ filtering techniques has been used to study changes in the intracellular sodium concentration in a variety of tissues using NMR spectroscopy [14, 15, 25-29, 30]. However, imaging extensions of these MQ techniques have been less common because of the weak nature of the MQ sodium NMR signal, which is typically only about 10-15% of the SQ sodium NMR signal. For example, Kalyanapuram et al. [31] obtained 3D TQ sodium MR images of the dog brain *in vivo* with data acquisition times of 105 minutes. A 105 minute scan is clearly not clinically feasible. However, using the TPI approach developed in our lab by Boada et al. [19], this thesis presents 3D TQ sodium MR images of the *in vivo* non-human primate brain acquired in 18 minutes.

# 2.0 THE IMPORTANCE OF SODIUM IN ACUTE STROKE

Stroke is the third largest cause of mortality in the United States, and it accounts for a significant portion of the country's health care expenditures because of the severe disabilities and long recovery periods that stroke survivors experience. Recently, the use of thrombolytic agents such as tissue plasminogen activator (tPA) has made it possible to reverse the ischemia that occurs in acute stroke. This therapeutic approach has proven to be effective in about 60% of subjects that are treated within 3-4 hours after the appearance of symptoms [32].

The effectiveness of tPA administration is highly dependent on the viability of the cells in the ischemic tissue (where "viable" is defined as "able to be recovered through reperfusion"). However, the 3-4 hour "clinical window of opportunity" does not adequately assess the viability of the ischemic tissue. This is because ischemic tissue damage depends on the combination of both the duration and the severity of the underlying cerebral blood flow (CBF) deficit. Within the ischemic tissue there could be several different regions with different CBF deficits and different amounts of damage, and even within the same region the CBF deficit could fluctuate over time. Tissue that is not severely underperfused can remain viable for times that extend well beyond the "clinical window of opportunity," while tissue that is severely underperfused remains viable for only a short time after ischemia onset.

Therefore, the development of a non-invasive method to ascertain the viability of ischemic tissue in acute stroke would allow the use of tPA in patients that do not meet the "clinical window of opportunity" but that still have a significant volume of viable tissue. Currently, there are no proven means to ascertain tissue viability using MRI or any other clinically available neuroimaging technique – MRI techniques such as perfusion imaging and diffusion weighted imaging can delineate the volume of ischemic tissue, but they are not able to differentiate whether the tissue is viable or non-viable [33]. Both perfusion imaging and diffusion weighted imaging are proton ($^1$H) MRI techniques. MRI of the $^1$H nucleus makes up the vast majority of all clinical MRI performed today [9]. MR imaging using other nuclei, such as the sodium nucleus, is still being developed, and is primarily only used in research studies. However, because of sodium's important role in ischemia, we hypothesize that the further development of sodium MRI could result in a valuable non-invasive diagnostic tool in acute stroke.

Normal brain cells maintain a large sodium ion concentration gradient across their membrane, with an intracellular sodium concentration of about 20mM and an extracellular sodium concentration of about 140mM [15]. This sodium concentration gradient is essential to many of the basic physiological functions of the cell [14]. The gradient is maintained by sodium-potassium-ATPase (Na-K-ATPase), which is an ion pump that splits ATP (adenosine tri-phosphate) in order to pump $Na^+$ out of the cell and $K^+$ into the cell. ATP is the cell's primary energy currency, and the maintenance of the large sodium concentration gradient by Na-K-ATPase requires a large proportion of the cell's ATP or energy [16, 19, 24].

Ischemia, such as that in acute stroke, causes abnormal or impaired energy metabolism, disturbing the Na-K-ATPase, and interrupting the continuous pumping of sodium out of the cell [16]. Therefore, very quickly after the onset of ischemia there is an increase in the intracellular sodium concentration (ISC), as shown by the cartoon diagram in Figure 2.1.

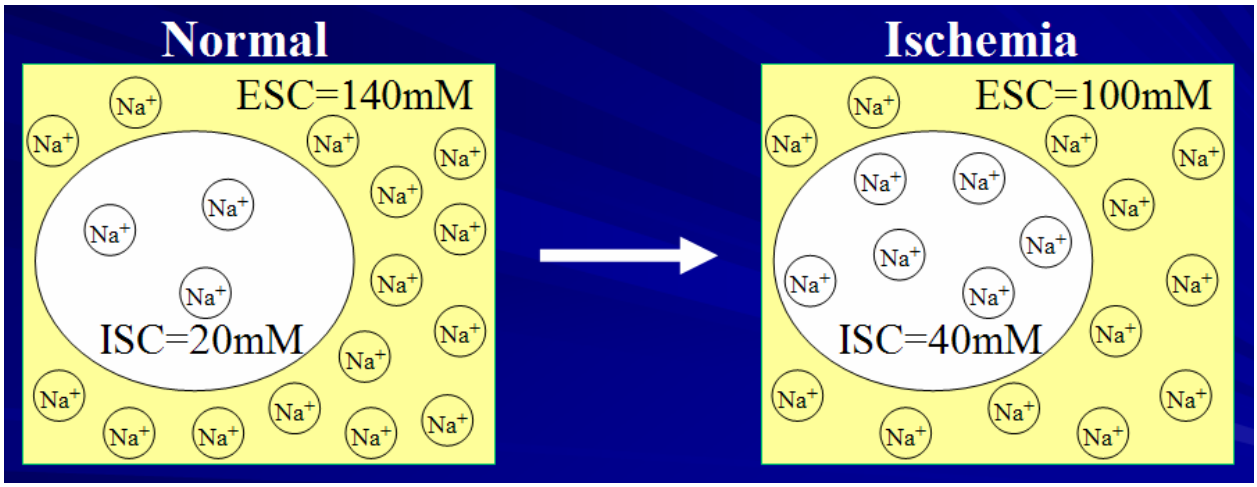


**Figure 2.1: Schematic Diagram of Influx of Sodium into the Cell that Occurs in Ischemia**
**Schematic diagram of the intracellular sodium concentration (ISC) and extracellular sodium concentration (ESC) in the normal brain (left) and very shortly after the onset of ischemia (right). Ischemia in acute stroke causes abnormal or impaired energy metabolism, disturbing the Na-K-ATPase, and interrupting the continuous pumping of sodium out of the cell. The result is that very quickly after the onset of ischemia there is an increase in ISC.**

In addition to the increase in ISC, it has been shown that the total tissue sodium concentration (TSC) gradually increases in ischemia [23, 34-42]. The mechanism for this TSC increase is not known for certain. However, it has been proposed that the intracellular sodium influx that occurs in ischemia creates an extracellular sodium gradient between the lesion and the

surrounding tissue, and in the presence of this gradient, sodium diffuses from the surrounding tissue into the lesion creating a gradual and continuous increase in TSC [36]. The increase in TSC in ischemia has been well-documented in the literature using mainly invasive measurements such as flame photometry in which each animal is sacrificed to provide data at a single time point after ischemia. The TSC increases observed in several animal models of cerebral ischemia (where MCAO is middle cerebral artery occlusion and CCAO is common carotid artery occlusion) are listed in Table 2.1 (where most of the information is from Table 3 of Wang et al. 2000 [35]).

**Table 2.1: Increases in TSC in Animal Models of Cerebral Ischemia**

| Reference | Species | Model | Normal Brain TSC | Ischemic Brain Slope of TSC ↑ mEq/kg dry weight/hr) or (%/hr) | |
|---|---|---|---|---|---|
| Dickenson and Betz (1992) | Rat | MCAO | 189 mEq/kg DW | 66.0 mEq/kg DW/hr | 34.9 %/hr |
| Schuier and Hossman (1980) | Cat | MCAO | 249 mEq/kg DW | 48.6 mEq/kg DW/hr | 19.5 %/hr |
| Young et al. (1987) | Rat | MCAO | 254 mEq/kg DW | 40.8 mEq/kg DW/hr | 16.1 %/hr |
| Ito et al. (1979) | Gerbil | CCAO | 230 mEq/kg DW | 58.8 mEq/kg DW/hr | 25.6 %/hr |
| Lo et al. (1987) | Gerbil | CCAO | 208 mEq/kg DW | 48.6 mEq/kg DW/hr | 23.4 %/hr |
| Betz et al. (1994) | Rat | MCAO | … | 42.6 mEq/kg DW/hr | … |
| Wang et al. (2000) | Rat | MCAO+ biCCAO | 248 mEq/kg DW | 57.0 mEq/kg DW/hr | 23.0 %/hr |
| Thulborn et al. (1999) | Monkey (n = 1) | MCAO | 45 mM | 5.7mM/hr | 12.7 %/hr |

These studies [23, 34-42] indicate that the increase in TSC in ischemia is linear in nature, and support the existence of a time course for TSC in MCA occlusion in small laboratory animals as depicted in Figure 2.2. Figure 2.2 also demonstrates the general consensus in the literature that in small laboratory animals there is a three hour time window during which ischemic damage may be reversed by tissue reperfusion [43, 44]. This time window of opportunity for improvement upon tissue reperfusion is known to be quite short (≤ 3 hours) for small laboratory animals [43, 44], possibly due to high cerebral metabolic rates and relatively poor collateral circulation, and slightly longer for larger animals [45, 46].

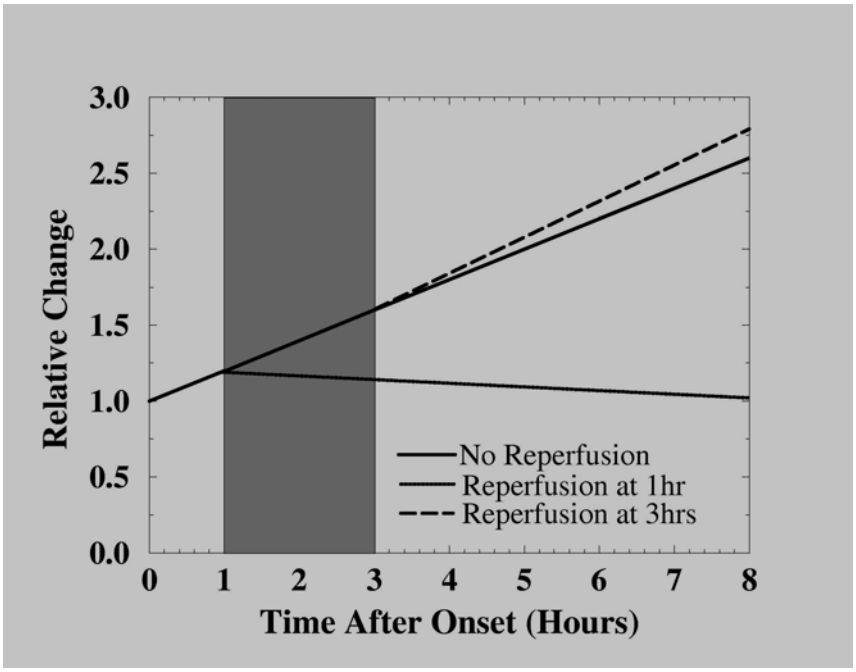


**Figure 2.2: Time Course of TSC after Brain Ischemia in Small Laboratory Animals**
**The TSC time course after brain ischemia in small laboratory showing the estimated three hour time window during which reperfusion will result in reversal of the ischemic damage.**

Because of the facts discussed previously, there are a number of features that make the non-invasive assessment of TSC and ISC during ischemia a useful tool for the diagnosis and treatment of acute stroke. First, because of the linear increase in TSC, there should be a threshold of TSC such that if the tissue goes above that threshold it cannot be recovered. Second, because the increase in ISC is more sudden compared to the slow, gradual diffusion-mediated TSC increase, ISC might provide an earlier indication of tissue fate than TSC. In other words, because the TSC increase lags behind the increase in ISC, monitoring the ISC changes might identify the extent of the ischemic tissue and perhaps even indicate its viability earlier than is possible with TSC. In this thesis, we investigate the spatial distribution and time evolution of these quantities in a non-human primate model of reversible focal brain ischemia by performing single quantum (SQ) sodium MRI to study the increase in TSC on a pixel by pixel basis, and by performing triple quantum (TQ) sodium MRI to study the changes in ISC.

# 3.0 NON-HUMAN PRIMATE MODEL OF REVERSIBLE FOCAL BRAIN ISCHEMIA

Many reports in the literature have studied the increase in the tissue sodium concentration (TSC) that occurs during acute stroke using small animal models of brain ischemia [34-41]. However, most of these studies used invasive direct tissue analysis with flame photometry in which each animal provided data at only a single time point. Therefore, these studies did not allow the characterization of the tissue sodium concentration (TSC) over the time course of the stroke in individual animals. This thesis presents sodium MRI as an *in vivo* means for non-invasively characterizing TSC over the time course of acute stroke in individual animals. Furthermore, in small animal models of brain ischemia [34-41], the size of the brain is much smaller and the cerebral metabolic rates are higher than in humans. Therefore, an endovascular model of non-human primate reversible focal brain ischemia was developed in our lab by Jungreis et al. [47] in order to provide a model that would be closer to humans in brain size and metabolic rate, as well as to provide the necessary spatial and temporal resolution for the sodium MRI studies.

In this non-human primate model, ischemia is achieved endovascularly using embolization coils to occlude the posterior cerebral artery (PCA) and a balloon catheter to occlude the middle cerebral artery (MCA) on the right hemisphere of the animals (schematic diagram shown in Figure 3.1). (Please note that all images in this thesis are shown in radiological orientation so that the left side of the image is the right side of the brain, and vice versa.) These non-human primate experiments are a collaboration with Dr. Charles Jungreis in

the Department of Radiology at Temple University and Dr. Edwin Nemoto in the Department of Radiology at the University of Pittsburgh. This collaboration takes advantage of Dr. Jungreis' pediatric interventional radiology expertise in performing neurocatheterization on non-human primates as well as the expertise of Dr. Nemoto in performing and maintaining anesthetization on non-human primates.

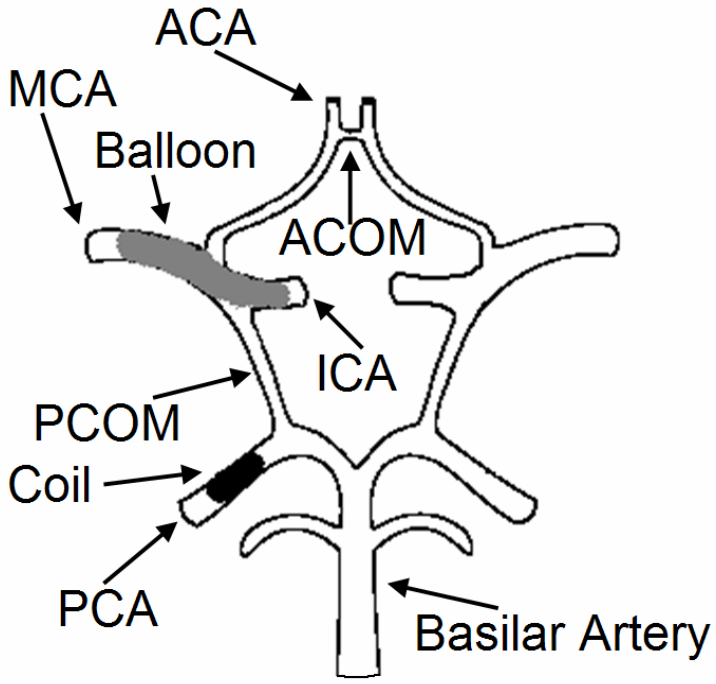


**Figure 3.1: Schematic Diagram of Non-Human Primate Endovascular Occlusion Model**
**Schematic diagram of the inferior view of the cerebral vasculature after endovascular occlusion, showing the positions of the balloon catheter (gray) occluding the right MCA and the embolization coils (black) occluding the right PCA.**

## 3.1 ANIMAL PREPARATION

Under a protocol approved by the Institutional Animal Care and Use Committee (IACUC), each pig-tail monkey (*Maccaca nemestrina*) is anesthetized with ketamine (10 mg/kg IM), and transported in a covered pediatric incubator from the animal holding facility on the 8$^{th}$ floor of the Division of Laboratory Animal Resources (DLAR) using the "soiled" elevator to the 2$^{nd}$ floor, and from there to the elevators to the B-floor of BST north tower. From the B-floor, the animal is transported over the bridge to the 5$^{th}$ floor of Scaife Hall, from which it is transported using the freight elevators to the basement of Scaife Hall. In the basement, the animal is

transported to the UPMC Presbyterian B-wing freight elevators (dock entrance) to the animal laboratory of the UPMC Magnetic Resonance Research Center (MRRC) in rooms B–844 and B-844.1.

In the animal laboratory of the MRRC, the animal is transferred from the pediatric incubator to the home-built table which travels with the animal throughout the next 12 hours of the protocol. Next, the animal is intubated and placed on a mechanical respirator. A peripheral intravenous (IV) catheter is placed, and the animal is maintained under anesthesia throughout the experiment using an IV fentanyl infusion (25 μg/kg/h). In addition, normal saline is administered IV at a rate of 5 mL/kg/h for the replacement of fluids. The animal is also paralyzed with 0.06 mg/kg/h pancuronium bromide. The animal's body and head are individually secured to the table, which was custom-built so that the animal can be safely transported with the head immobilized, and also has built-in sodium calibration standards which will be discussed later. Extreme care is taken in completely securing the position of the animal's head to the table so that the head remains immobilized on the custom-built table as the table is transported to the angiography suite for the endovascular procedure, and then back to the MRRC where it is slid onto its custom-built platform in the 3T MRI magnet. Figure 3.2 shows the custom-built table in the animal laboratory of the MRRC, where the animal is intubated and the IV catheter is placed, and on which the animal is positioned and secured for the rest of the protocol.

**Figure 3.2: Custom-Built Table with Sodium Standards in MRRC Animal Laboratory**
**The custom-built table with built-in sodium calibration standards in the animal laboratory of the MRRC, where the animal is intubated and the IV catheter is placed, and on which the animal is positioned and secured for the rest of the protocol.**

The animal's temperature is maintained at 37$^{o}$C using a recirculating hot water blanket, and the animal's blood pressure (BP) and exhaled gases are monitored continuously using the MR compatible monitor shown in Figure 3.3 (MEDRAD, Indianola, PA). Next, the animal is transported from the MRRC via the UPMC Presbyterian B-wing freight elevators to the loading dock, and then by the back corridors to the back of the angiography suite and into the special procedures room (angiography suite room E190).


**Figure 3.3: MR Compatible Monitor for Measuring Blood Pressure and Exhaled Gases**

## 3.2 ENDOVASCULAR PROCEDURE

In the angiography suite, Dr. Jungreis surgically exposes the animal's femoral artery, and using a standard 18-gauge angiographic puncture needle, introduces a 0.038" guidewire into the femoral artery. A 10-cm 5F or 6F vascular sheath is then passed over the guidewire and secured. Next, a 5F cerebral catheter (Merit Medical Systems, South Jordan, UT) is introduced through the sheath. Dr. Jungreis performs live subtraction fluoroscopy guided catheter manipulations to advance the cerebral catheter into the more accessible of the two vertebral arteries. Then, a microcatheter (Tracker 18 Turbo, Target Therapeutics, Fremont, CA) is coaxially inserted through the base catheter, and via the vertebrobasilar system into the right PCA distal to the posterior communicating artery. Endovascular embolization coils (Cook, Bloomington, IN) are deposited to occlude the right PCA at this level. Figure 3.4 shows Dr. Jungreis performing the endovascular procedure on a non-human primate in the angiography suite. Figure 3.5 shows a picture of the endovascular embolization coils (Cook, Bloomington, IN) used to occlude the right PCA.

**Figure 3.4: Dr. Jungreis Performing the Endovascular Procedure in Angiography Suite**

Next, the base catheter is positioned into the right internal carotid artery (ICA). At this point, the animal is systemically anticoagulated with an initial IV bolus of 500 Units of heparin followed by an IV heparin infusion of 100 Units/hr. Activated clotting time is used to monitor anticoagulation. The standard catheter is then exchanged for a guiding catheter (5F or 6F Envoy, Cordis Corporation, Miami, FL). We learned through preliminary experiments to cut about an inch off of the end of this guiding catheter because it contains metal that causes large image artifacts in the MRI studies. A non-detachable endovascular balloon (Endeavor NDSB 8501; Target Therapeutics, Fremont, CA) is then coaxially inserted through the guiding catheter. The balloon advanced further into the ICA and positioned at the origination of the MCA from the

circle of Willis. The balloon is inflated to achieve occlusion of the right MCA which is confirmed by angiography through the guiding catheter. We learned through preliminary experiments to get all air bubbles out of the balloon catheter prior to endovascular insertion because the bubbles cause image artifacts in the MRI studies. At this point, the endovascular procedure is complete. Thus, the catheter system is secured into position, and the MCA occlusion verified by angiography again prior to transport of the animal back to the MRRC.

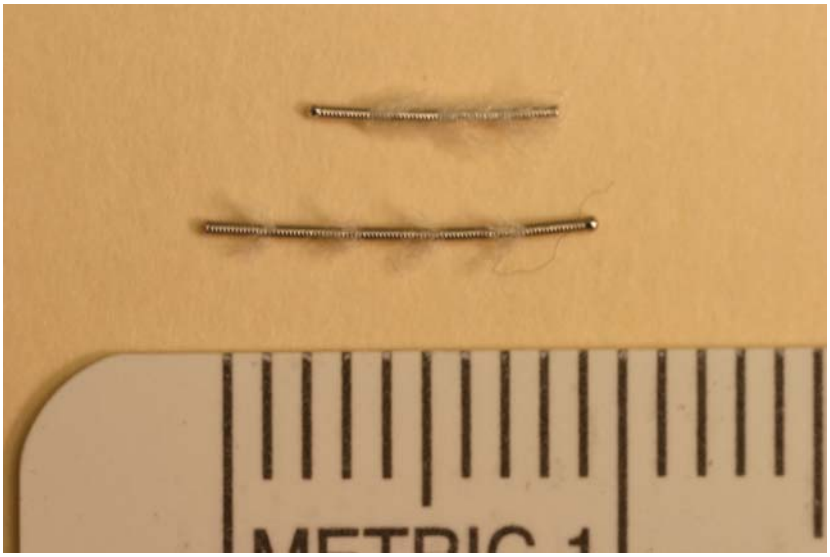

**Figure 3.5: Endovascular Embolization Coils used to Occlude the Right PCA**

## 3.3 TRANSFER TO THE 3T SCANNER FOR MRI STUDIES

The animal is then transferred by the same route back to the 8$^{th}$ floor, and into the magnet room of the MRRC's 3.0 Tesla whole body scanner (General Electric Medical Systems, Milwaukee, WI). The custom-built table carrying the animal is slid onto its custom-built platform in the 3T MRI magnet. The custom-built platform and table allow the non-human primate radiofrequency

(RF) head coils to be slid into place around the animal's head and removed without moving the positions of the animal's head and body. Thus, the position of the animal's head does not change throughout the entire angiography suite and MRI portions of the experiment, which is important for not changing the position of the balloon catheter in the MCA. The custom-built table and platform configuration also place the animal's head exactly at the isocenter of the 3T MRI magnet. Figure 3.6 (left) shows a picture of the custom-built platform and table with a phantom in one of the non-human primate RF head coils setup on the 3T MRI magnet for MR sequence testing purposes, and Figure 3.6 (right) shows the same setup with a non-human primate (although covered with blankets) as well as the anesthesia, BP, and ventilation lines.

**Figure 3.6: Non-Human Primate and Custom-Built Table/Platform Setup in 3.0T Scanner (left) The custom-built platform and table providing the proper positioning of a phantom in one of the non-human primate RF head coils setup on the 3T scanner for MR sequence testing purposes. (right) The same setup with a non-human primate (although covered with blankets) including all of the anesthesia, BP, and ventilation lines necessary for the experiment.**

Proton time of flight magnetic resonance angiography (MRA) scans (FOV = 16cm, TE = 4.7ms, TR = 35ms, $\theta = 25°$) are performed to verify that both the PCA and MCA on the animal's right hemisphere are still occluded after the transfer of the animal from the angiography suite (Figure 3.7 left). This non-human primate model of focal brain ischemia is reversible because after several hours of ischemia the balloon catheter in the right MCA can be deflated and removed to achieve reperfusion. The effectiveness of this reversible model of focal brain ischemia is shown in Figure 3.7 where proton MRA's are shown before (left) and after (right) reperfusion of the right MCA through deflation and removal of the balloon catheter in the right MCA. (Please note again that all images in this thesis are shown in radiological orientation so that the left side of the image is the right side of the brain, and vice versa.) The MRA in Figure 3.7 (left) demonstrates blood flow in the MCA and PCA on the left side of the brain, but no blood flow in the MCA and PCA on the right side of the brain. Thus, the right MCA and right PCA have been successfully occluded by the endovascular procedure. Then, reperfusion of the right MCA is achieved through deflation and removal of the balloon catheter in the right MCA at 3.5 hours after the onset of ischemia. Figure 3.7 (right) shows an MRA after this reperfusion, which demonstrates that blood flow has returned in the right MCA.

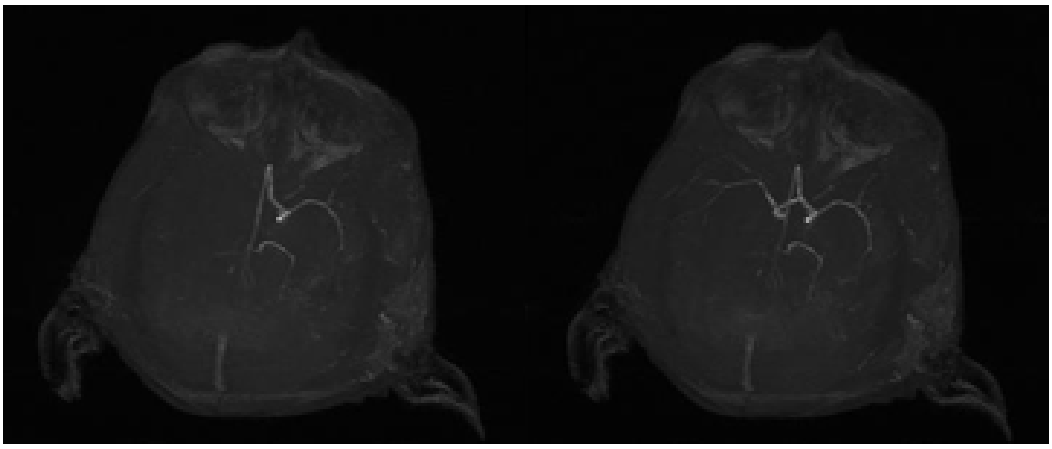

**Figure 3.7: Proton MRA's Before and After Reperfusion in Reversible Ischemia Model (left) Proton MRA acquired after endovascular occlusion of the right PCA and MCA. The MRA demonstrates blood flow in the MCA and PCA on the left side of the brain, but no blood flow in both the right MCA and right PCA. Thus, the right MCA and right PCA have been successfully occluded by the endovascular procedure. Then, reperfusion of the right MCA is achieved through deflation and removal of the balloon catheter in the right MCA at 3.5 hours after the onset of ischemia. (right) Proton MRA after this reperfusion, which demonstrates that blood flow has returned in the right MCA.**

# 4.0 THICK TISSUE SECTION MAP2 IMMUNOSTAINING FOR MACROSCOPIC DELINEATION OF INFARCT REGION IN THE NON-HUMAN PRIMATE BRAIN AT EARLY TIME POINTS AFTER STROKE

## 4.1 ABSTRACT

This study developed a protocol for the histological delineation of the infarct region over the entire non-human primate brain at early time points after ischemic stroke when triphenyl tetrazolium chloride (TTC) staining cannot clearly delineate the infarction region. In the compact rat brain, this early infarct delineation can be done by microtubule associated protein 2 (MAP2) immunostaining of thin (20-50μm) brain tissue sections; however, in the non-human primate the thin (20-50μm) brain tissue section MAP2 immunostaining protocol has difficulties and limitations that make it inadequate for the delineation of the infarct region over the entire brain. Therefore, we developed a thick (1-2.4mm) brain tissue section MAP2 immunostaining protocol for the delineation of the infarct region over the entire non-human primate brain. The increased durability of the thick brain tissue sections better maintained the integrity of the structure and shape of each section throughout the extensive MAP2 immunostaining procedure. Consequently, images of the resulting intact thick 2D brain tissue sections can then be stacked into a 3D volume of the non-human primate brain. Thus, the goal of this study was met: the

thick (1-2.4mm) brain tissue section MAP2 immunostaining protocol successfully allows the histological delineation of the infarct region over the entire brain at early time points in a non-human primate model of ischemic stroke.

## 4.2 INTRODUCTION

The goal of this study was to develop a protocol for the histological delineation of the infarct region over the entire non-human primate brain at early time points after ischemic stroke when TTC staining cannot clearly delineate the infarction area [48-51]. Previous reports have shown that the histological delineation of ischemic brain lesions at early time points after ischemic stroke can be achieved by immunohistochemical staining of thin (20-50μm) brain tissue sections with antibodies to microtubule associated protein 2 (MAP2) [52-54]. There is a reduction of MAP2 immunostaining in the ischemic lesion, and this reduction in MAP2 immunostaining has been shown to be a reliable marker of neurons that have already started down an irreversible path ultimately leading to cell death [52]. MAP2 immunostaining has been shown to be sensitive to both global [55, 56] and focal [52, 57] ischemia.

Several studies have successfully used MAP2 immunostaining of thin (20-50μm) tissue sections to measure the volume of the ischemic lesion across the entire brain in rats [52-54]. The MAP2 immunostaining protocol requires more than 24 hours of rotation of these free-floating brain tissue sections in different solution rinses and antibody solution incubations on a standard laboratory rotator. For the rather compact rat brain, these thin (20-50μm) tissue sections tolerate this protocol quite well and remain intact, allowing the resulting delineation of the infarct region over the entire brain. However, for the non-human primate brain, these thin tissue sections have

a much larger and more complicated shape (due to the lobe structure and the folds and sulci of the non-human primate brain). Therefore, during the brain cutting procedure these thin sections tend to disintegrate. The free floating immunostaining procedure considerably increases the damage: these thin tissue sections fold, tear, fray, and break apart. This renders the delineation of the infarct region over the entire brain from the MAP2 immunostaining of these thin tissue sections unworkable. Therefore, an alternative to the thin tissue section MAP2 immunostaining method for delineation of the infarct region over the entire brain was needed for our study involving a non-human primate model of focal brain ischemia. Consequently, our lab developed the following method of performing the MAP2 immunostaining protocol on thick (1-2.4mm) brain tissue sections.

## 4.3 METHODS

These experiments are a collaboration with Dr. Stephen Jones and Dr. Alexander Kharlamov in the Department of Anesthesiology at the Allegheny-Singer Research Institute in Pittsburgh, Pennsylvania. This collaboration takes advantage of the expertise of Dr.'s Jones and Kharlamov in thin (20-50μm) tissue section MAP2 immunohistochemical staining of rat focal brain ischemia.

### 4.3.1 Non-Human Primate Model of Brain Ischemia

Under a protocol approved by the Institutional Animal Care and Use Committee (IACUC), focal brain ischemia was induced in pig-tail monkeys (*Maccaca nemestrina*, n=4) using the endovascular model described in detail in Chapter 2 of this thesis. Using this model, ischemia

was achieved using embolization coils to occlude the posterior cerebral artery (PCA) and a balloon catheter to occlude the middle cerebral artery (MCA) on the right hemisphere of the animals. Deflation and removal of the balloon catheter in the right MCA was performed at a time between 3.5 and 5.4 hours after the onset of ischemia. Then, approximately 4 hours after deflation and removal of the balloon catheter in the right MCA for reperfusion of that artery, the non-human primates were sacrificed and the brains were fixed with 4% paraformaldehyde solution through transcardial perfusion, followed by immersion in 4% paraformaldehyde solution.

### 4.3.2 Rat Model of Brain Ischemia

Under a protocol approved by the Institutional Animal Care and Use Committee (IACUC), ischemia was induced in the male Sprague Dawley rat using a suture model of focal brain ischemia [58, 59]. Using this model, ischemia was achieved by inserting a lubricated 4-0 monofilament suture into the right common carotid artery and advancing the suture into the internal carotid artery up to the origination of the MCA from the circle of Willis. Four hours after the onset of ischemia the rat was sacrificed, and the rat brain was immediately removed and fixed by immersion in 4% paraformaldehyde solution.

### 4.3.3 Brain Cutting Procedure

Prior to cutting, the brains were removed from the 4% paraformaldehyde solution and placed in 30% sucrose solution for at least one week until complete saturation with sucrose. The brains were then removed from the 30% sucrose solution, frozen on dry ice, and cut using a Hisotoslide

2000 sliding microtome (Reichert-Jung, Nussloch, Germany) into either thin 50μm tissue sections or thick (1-2.4mm) tissue sections. Figure 4.1 shows a picture of the Reichert-Jung Histoslide 2000 sliding microtome that was bought specifically for these studies in order to be large enough to cut the non-human primate brains. After the cutting of the brain tissue sections, they were placed in cryoprotectant solution (30% ethylene glycol, 30% glycerin, and 40% 0.1 M phosphate buffer solution).

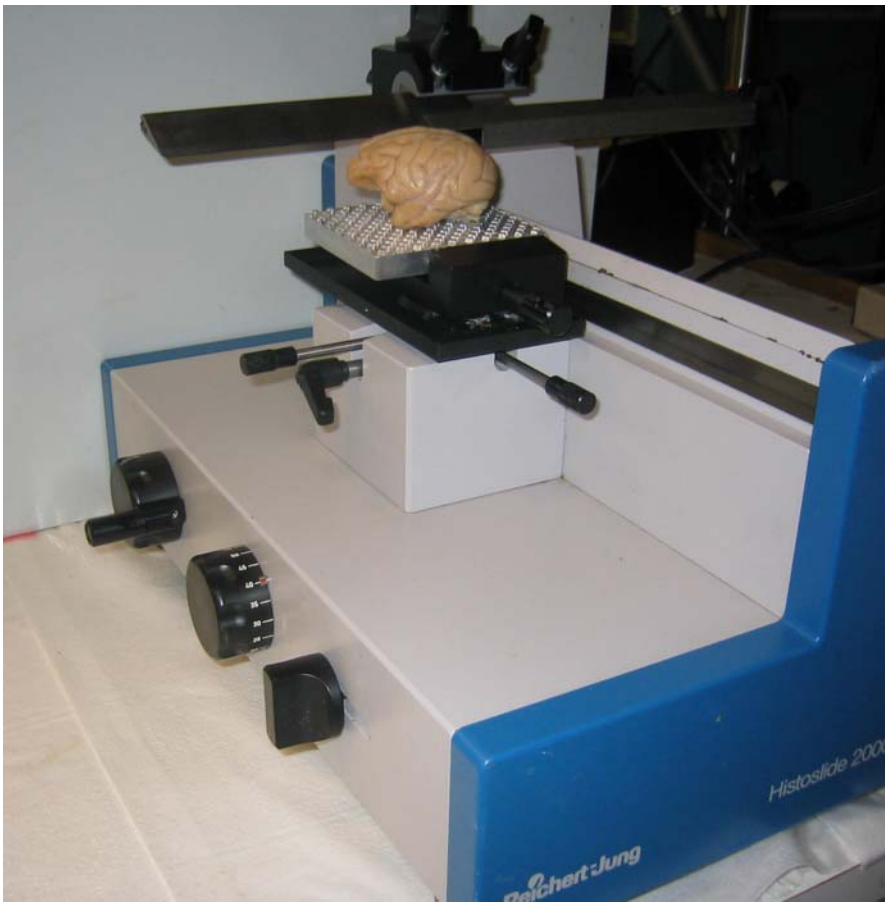


**Figure 4.1: Non-Human Primate Brain on Reichert-Jung Histoslide 2000 Microtome**

### 4.3.4 Immunohistochemical Procedure

Free-floating brain tissue sections that had been fixed in 4% paraformaldehyde solution were processed using the conventional avidin-biotinylated-peroxidase method with 3,3'-diaminobenzidine as the peroxidase substrate [60, 54]. The brain tissue sections were removed from the cryoprotectant solution and rinsed in 0.1 M phosphate buffer solution four times for 5 min per rinse. This was followed by a 30 min incubation in 0.6% hydrogen peroxide in phosphate buffer solution, followed again by four 5 min rinses in 0.1 M phosphate buffer solution. (Note that all rinses were done with the free-floating brain tissue sections being rotated

in glass or ceramic dishes by a standard laboratory rotator.) Next, the tissue sections were rinsed in 0.1 M Tris-buffered saline (TBS, pH 7.4) containing 0.25% Triton X-100 (TBS + Triton) three times for 10 min per rinse. Then, the tissue sections were blocked by incubation for 30 min in TBS + Triton containing 3% goat serum. This was followed by two 10 min rinses in TBS + Triton. The tissue sections were then incubated overnight at 4°C with primary MAP2 antibodies (HM2 or AP20, Sigma, St. Louis, MO) diluted in TBS + Triton containing 1% goat serum (thin non-human primate brain sections, AP20 1:1000; thick non-human primate brain sections, HM2 1:1000; all rat brain sections HM2 1:1500).

Upon removal from the overnight primary MAP2 antibody incubation, the tissue sections were rinsed in TBS containing 1% goat serum two times for 10 min per rinse. Then, the tissue sections were incubated for 1 hour at room temperature in biotinylated goat anti-mouse secondary IgG (1:500, Jackson ImmunoResearch Laboratories Inc., West Grove, PA) in TBS containing 1% goat serum. This was followed by three 10 min rinses in TBS. The tissue sections were then incubated for 1 hour in avidin-biotinylated-peroxidase complex (ABC Elite kit, Vector Laboratories, Burlingame, CA). This was followed by a 10 min rinse in TBS and then two 10 min rinses in imidazole acetate buffer (pH 7.4). Sections were then treated with imidazole acetate buffer (pH 9.6) containing 0.05% diaminobenzidine, 2.5% nickel ammonium sulfate, and 0.005% $H_20_2$ for 6-10 minutes until adequate staining of the tissue sections was achieved. This was followed by a 10 min rinse in imidazole acetate buffer (pH 7.4) and three final 5 min rinses in 0.1 M phosphate buffer solution. As controls for non-specific staining, sections were processed through all steps above with omission of either the primary antibody or the secondary antibody. The thin MAP2 immunostained sections were mounted onto gelatin-coated glass slides, examined under light microscopy, and their images digitized by a

slide scanner (Nikon, LS-2000) using a medical slide holder (Nikon, FJ-G1). Images of the thick MAP2 immunostained sections were digitized on a high resolution HP scanner (HP Scanjet 4570C).

## 4.4 RESULTS AND DISCUSSION

First, the MAP2 immunostaining protocol was performed on thin 50μm axial non-human primate brain sections, and Figure 4.2 shows one of these sections. Figure 4.2 demonstrates that the thin non-human primate brain sections, although they have a specific MAP2 immunostaining, have a large and complicated shape and these sections tear, pieces of the sections break off, and the edges of the sections fray during the MAP2 immunostaining protocol. Clearly, the delineation of an infarct region over the entire non-human primate brain from these thin MAP2 immunostained tissue sections is not practical.

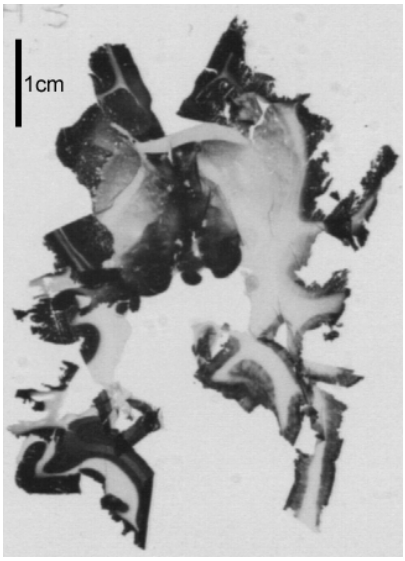


**Figure 4.2: MAP2 Immunostaining of Thin 50μm Non-Human Primate Brain Section**
**MAP2 immunostaining protocol performed on thin 50μm axial non-human primate brain section. The thin non-human primate brain sections have a large and complicated shape and these sections tear, pieces of the sections break off, and the edges of the sections fray during the MAP2 immunostaining protocol.**

Our hypothesis was that performing the MAP2 immunostaining protocol on thick (1-2.4mm) non-human primate brain sections would allow the tissue sections to remain much more intact so that delineation of the infarct region could be achieved in each slice, and then images of the slices could be stacked into a 3D volume. However, the question remained as to whether MAP2 immunostaining of thick (1-2.4mm) sections would adequately delineate the infarct region the way that MAP2 immunostaining of thin (20-50μm) sections did. Therefore, this was tested in a suture model of focal brain ischemia in the rat. The MAP2 immunostaining protocol was performed on alternating thick 1mm sections and thin 50μm sections of the rat brain after 4 hours of right-sided focal brain ischemia. Figure 4.3 shows a resulting MAP2 immunostained thick 1mm rat brain section (top) and the adjacent thin 50μm rat brain section (bottom) from this

4-hour right-sided focal brain ischemia experiment. Decreased MAP2 immunostaining indicating the infarct region can be seen in both the thick (top) and thin (bottom) sections on the right side of the brain (left side of the images). Qualitatively, the location and shape of the infarct region can be seen to be the same for both the thick 1mm section and the thin 50μm section. Measuring the infarct region areas in the two sections using the medical image analysis program Amide [61], the infarct area of the thick 1mm section was 98±2% of the infarct area of the thin 50μm section, demonstrating good quantitative agreement between the two sections. Thus, the MAP2 immunostaining of the thick rat brain sections successfully allows the delineation of the infarct region equally as well as the thin rat brain sections. In addition, the increased durability of the thick brain sections better allows the maintenance of the structure and shape of each section throughout the MAP2 immunostaining procedure. Consequently, the 2D images of the thick brain sections (demonstrating the infarct region in each section) can more easily be stacked into a 3D volume of the entire MAP2 immunostained brain.

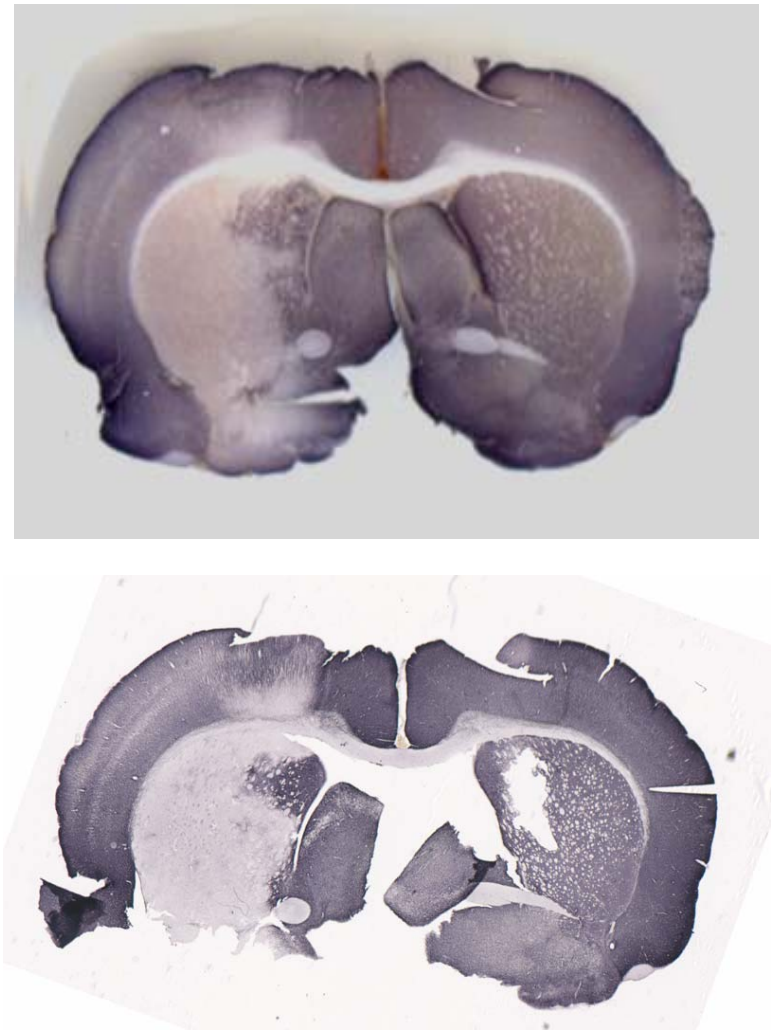

**Figure 4.3: Comparison of Thick and Thin MAP2 Immunostained Rat Brain Sections**

**MAP2 immunostaining of (top) thick 1mm rat brain section and (bottom) adjacent thin 50μm rat brain section after 4 hours of right-sided focal brain ischemia. Decreased staining can be seen in the infarct region on the right side of the brain (left side of the images) in both the thick and thin sections. Qualitatively, the location and shape of the infarct region can be seen to be the same for both the thick 1mm section and the thin 50μm section. Measuring the infarct region areas in the two sections, the infarct area of the thick 1mm section was 98±2% of the infarct area of the thin 50μm section. The increased durability of the thick brain sections better allows the maintenance of the structure and shape of each section throughout the MAP2 immunostaining procedure, so that the 2D images of the slices can then be stacked into a 3D volume of the entire MAP2 immunostained brain.**

Next, this thick (1-2.4mm) brain tissue section MAP2 immunostaining protocol was tested on non-human primate stroke brains (n = 4). The resulting thick 2.4mm MAP2 immunostained sections for one non-human primate stroke brain are shown in Figure 4.4. In this non-human primate, the right MCA and right PCA were occluded for a duration of 5.23 hours, at which point reperfusion of the right MCA was achieved through deflation and removal of the balloon catheter, and approximately 4 hours later the animal was sacrificed and the brain fixed through transcardial perfusion with 4% paraformaldehyde solution. The fifteen 2.4mm thick MAP2 immunostained coronal tissue sections represent every other section through the brain starting with section "1" as the most caudal section and ending with section "15" as the most rostral section. In sections 1 and 2, the decreased MAP2 immunostaining indicating the infarct region can be seen to cover the entire right hemisphere of the brain (left side of the images). Moving anteriorly, in sections 3 through 5 the infarct region gradually covers only the inferior half of the right hemisphere, in sections 6 through 10 the infarct region gradually covers a smaller and smaller fraction of the inferior and medial portions of the right hemisphere, until there is no infarct region in sections 11 through 15. In the non-human primate brain, the thick (1-2.4mm) MAP2 immunostaining protocol allows the tissue sections to remain intact so that the successful delineation of the infarct region can be achieved in each slice through the brain.

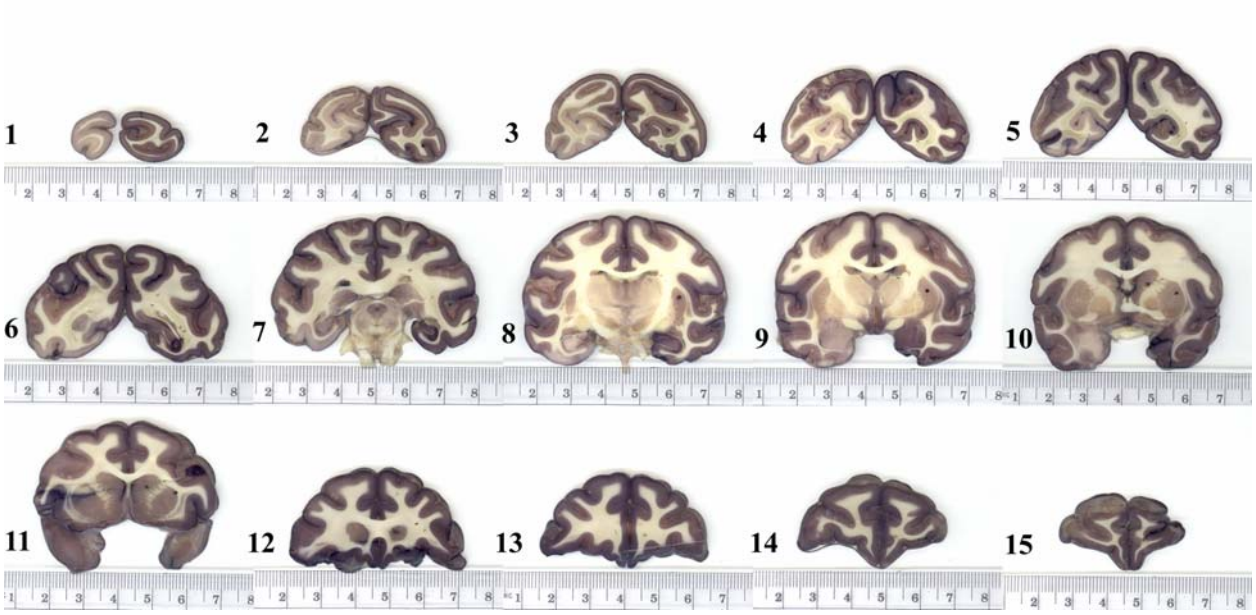


**Figure 4.4: Thick 2.4mm MAP2 Immunostaining of Entire Non-Human Primate Brain**

**Fifteen 2.4mm thick MAP2 immunostained sections through one non-human primate stroke brain. These fifteen 2.4mm thick MAP2 immunostained coronal tissue sections represent every other section through the brain starting with section "1" as the most caudal section and ending with section "15" as the most rostral section. In sections 1 and 2, the decreased MAP2 immunostaining indicating the infarct region can be seen to cover the entire right hemisphere of the brain (left side of the images). Moving anteriorly, in sections 3 through 5 the infarct region gradually covers only the inferior half of the right hemisphere, in sections 6 through 10 the infarct region gradually covers a smaller and smaller fraction of the inferior and medial portions of the right hemisphere, until there is no infarct region in sections 11 through 15.**

## 4.5 CONCLUSIONS

The goal of this study was to develop a protocol for the histological delineation of the infarct region over the entire brain at early time points in a non-human primate model of ischemic stroke. In the compact rat brain, this can be done by MAP2 immunostaining of thin (20-50μm) brain tissue sections [52-54]; however, in the non-human primate the thin (20-50μm) brain tissue section MAP2 immunostaining protocol has difficulties and limitations that make it inadequate for the delineation of the infarct region over the entire brain. Therefore, we developed a thick (1-2.4mm) brain tissue section MAP2 immunostaining protocol for the delineation of the infarct region over the entire non-human primate brain. The increased durability of the thick brain tissue sections better maintains the integrity of the structure and shape of each section throughout the extensive MAP2 immunostaining procedure. Thus, the goal of this study was met: the thick (1-2.4mm) brain tissue section MAP2 immunostaining protocol successfully allows the histological delineation of the infarct region over the entire brain at early time points in a non-human primate model of ischemic stroke.

# 5.0 SINGLE QUANTUM SODIUM MRI OF NON-HUMAN PRIMATE REVERSIBLE FOCAL BRAIN ISCHEMIA

## 5.1 ABSTRACT

In the United States, stroke is the third leading cause of mortality and one of the major causes of serious, long-term disability among adults. The introduction of thrombolytic therapy using tissue plasminogen activator (tPA) has revolutionized the treatment of acute stroke by providing an aggressive means for the reversal of the ischemic insult, albeit with potential complications that require eligibility criteria relying heavily on the time since the onset of symptoms "clinical window of opportunity" [32]. Because of the steady and continuous increase in tissue sodium concentration (TSC) that occurs in acute stroke, sodium MRI has been proposed as a means to help extend the use of tPA to patients that do not meet the "clinical window of opportunity" [35]. We hypothesize that the rate of TSC increase can vary from patient to patient, and can also vary within the ischemic tissue of a single patient. We believe that using sodium MRI to measure the rates of TSC increase in the ischemic tissue could provide information regarding tPA administration based on whether a significant volume of tissue has only seen mild increases in TSC. To that end, we demonstrate the use of single quantum (SQ) sodium MRI for measuring the time course of TSC in a reversible, non-human primate model of focal brain ischemia. Our

results indicate that TSC increases linearly in the ischemic tissue during arterial occlusion, that the rate of this TSC increase varies across the lesion, and that markedly different time courses of TSC ensue after restoration of blood flow.

## 5.2 INTRODUCTION

As the third largest cause of mortality in the United States, stroke accounts for a significant portion of the country's health care expenditures. Recently, the use of thrombolytic agents such as tissue tPA has made it possible to reverse the ischemia that occurs in acute stroke. This therapeutic approach has proven to be effective in about 60% of subjects that are treated within 3-4 hours after the appearance of symptoms; however only a small percentage of patients actually receive thrombolytic therapy [32]. This is because the clinical use of thrombolytic therapy requires eligibility criteria relying heavily on the "three hour" time limit since the onset of symptoms [32]. Sodium MRI has been proposed as a means to help extend the use of tPA to patients that do not meet this eligibility criteria [35].

Increasing total tissue sodium concentration (TSC) during focal brain ischemia has been well documented in the literature [23, 34-42]. The eight animal model studies of cerebral ischemia listed in Table 2.1 found TSC increases ranging from 16%/hour to 35%/hour for small animal models and a TSC increase of 12.7%/hour for a single non-human primate [34-40, 42]. We hypothesize that because ischemia is associated with time-dependent increases in TSC, the further development of sodium MRI for non-invasively measuring TSC in ischemic tissue could result in a valuable diagnostic tool in acute stroke.

## 5.3 METHODS

### 5.3.1 Animal Preparation

Under a protocol approved by the Institutional Animal Care and Use Committee (IACUC), focal brain ischemia was induced in pig-tail monkeys (*Maccaca nemestrina*, n=4) using the endovascular model described in detail in Chapter 2 of this thesis. Using this model, ischemia was achieved using embolization coils to occlude the posterior cerebral artery (PCA) and a balloon catheter to occlude the middle cerebral artery (MCA) on the right hemisphere of the animals.

### 5.3.2 MR Imaging

The *in vi*vo MRI studies were performed on the MRRC's 3 Tesla whole body scanner (General Electric Medical Systems, Milwaukee, WI) using $^{23}$Na and $^{1}$H quadrature birdcage RF coils custom-built to fit the animals (AIRI, Cleveland, OH). Proton time of flight magnetic resonance angiography (MRA) scans (FOV = 16cm, TE = 4.7ms, TR = 35ms, $\theta = 25°$) were performed to verify that both the PCA and MCA on the animal's right hemisphere were still occluded after the transfer of the animal from the angiography suite. Anatomical proton 3D spoiled gradient recalled (SPGR) images were also acquired for registration purposes (FOV = 16cm, TE = 15ms, TR = 35ms, $\theta = 25°$). Three-dimensional single quantum (SQ) sodium MR images were acquired throughout the duration of the experiment using a twisted projection imaging (TPI) sequence [19] with 816 scans, TE= 0.5ms, TR = 100ms, and NEX = 4 for a total SQ data acquisition time of 5.5 minutes. The SQ image intensities were calibrated to TSC using sodium calibration standards within the image field of view (40mM, 80mM, and 120mM NaCl in 10%

agarose). The reconstructed images were obtained by using a regridding algorithm (tri-linear kernel, window width one, no oversampling), producing a 64x64x64 stack for each image. The field of view (FOV) was 20x20x20cm, resulting in a voxel size or resolution of 3.125x3.125x3.125mm.

## 5.4 RESULTS AND DISCUSSION

The effectiveness of this reversible model of focal brain ischemia is shown in Figure 3.7 where proton MRA's are shown before (left) and after (right) reperfusion of the right MCA through deflation and removal of the balloon catheter in the right MCA. The MRA in Figure 3.7 (left) demonstrates blood flow in the MCA and PCA on the left side of the brain, but no blood flow in the MCA and PCA on the right side of the brain. Thus, the right MCA and right PCA have been successfully occluded by the endovascular procedure. Then reperfusion of the right MCA is achieved through deflation and removal of the balloon catheter in the right MCA (without removing the animal from the scanner) at 3.5 hours after the onset of ischemia. Figure 3.7 (right) shows an MRA after this reperfusion, which demonstrates that blood flow has returned in the right MCA.

Figure 5.1 demonstrates an example of one of the 5.5 minute 3D SQ sodium images, which are 64x64x64 voxels or pixels (although shown as separate 2D axial slices for viewing purposes). These SQ sodium images are acquired consecutively throughout the experiment.

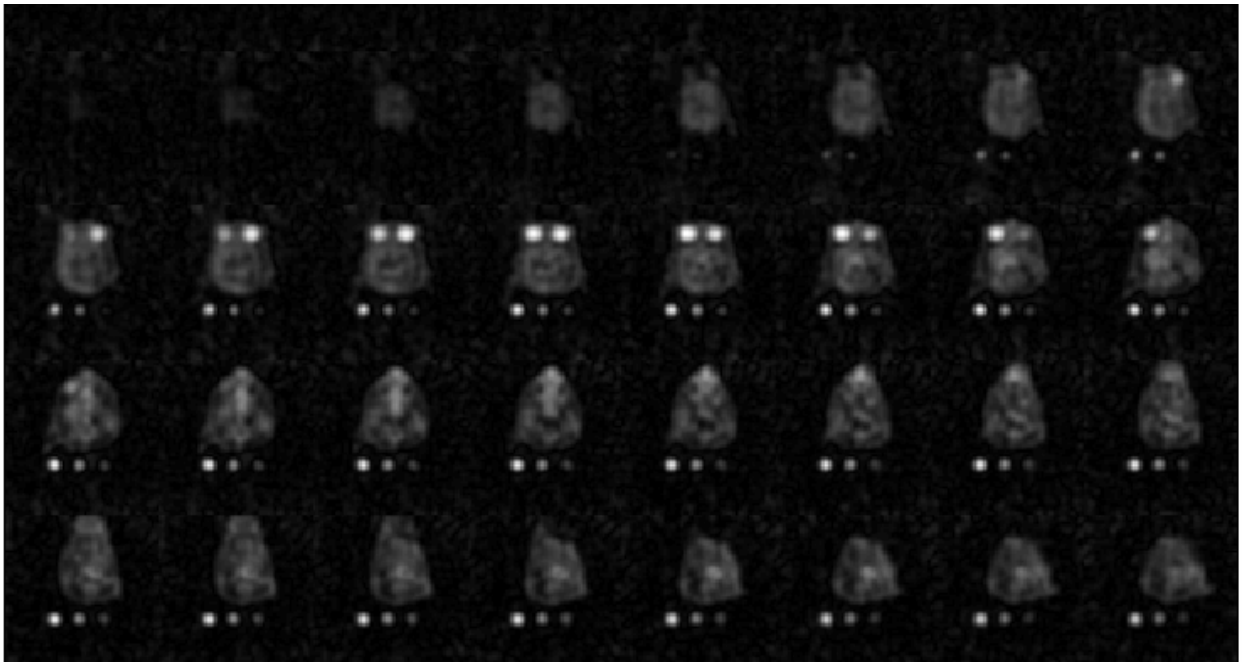

**Figure 5.1: A 5.5 minute 3D SQ Sodium MR Image of Non-Human Primate Brain**
**A 64 x 64 x 64 three-dimensional SQ sodium image is shown. However, to present it in 2D it is arbitrarily displayed as axial slices.**

The arbitrary image intensities are then converted to TSC using the sodium calibration standards within the image field of view. Therefore, if there are 24 images before reperfusion, then for each pixel there are 24 values of TSC that can be plotted versus time to examine the increasing TSC during ischemia. Both the literature [23, 34-42] and our results indicate that the increase in TSC in ischemia is linear in nature. However, the rate of this TSC increase can vary between pixels in the ischemic region of the same animal as well as between animals. Therefore, on a pixel by pixel basis, the TSC is plotted versus time and a linear regression analysis is performed to determine the slope of the TSC increase and to test this slope for statistical significance. This results in a TSC slope map, which is an image in which the pixel intensity

represents the time rate of change of TSC for that pixel. (See Appendix for TSC error propagation analysis and linear regression analysis with statistical significance testing.)

Figure 5.2 presents selected partitions from SQ sodium 3D MR images (top) and TSC slope maps before (middle) and after (bottom) reperfusion through deflation and removal of the balloon catheter in the right MCA. Notably, most of the changes in TSC accumulation rates take place in the MCA territory (indicated by the arrows) where a reduction in TSC increase is observed after reperfusion.

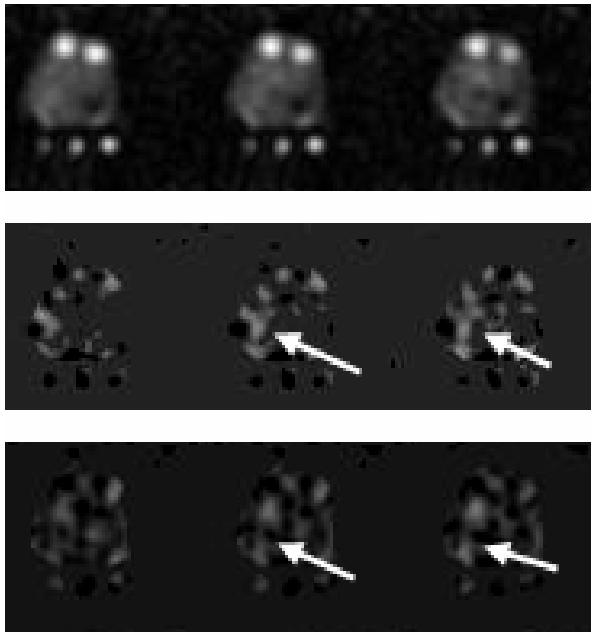

**Figure 5.2: 3D SQ Image and TSC Slope Maps Before and After Right MCA Reperfusion (top row) Selected partitions from a 3D SQ sodium MR image, and their corresponding TSC slope maps before (middle row) and after (bottom row) reperfusion of the right MCA. Changes in the rate of TSC accumulation are clearly observed in the region corresponding to the MCA territory (arrows). Only pixels with statistically significant slopes are shown in these maps.**

Next, all of the image data was imported into the AMIDE [61] medical image software package in order to view multiple data sets at once. Registration of the sodium images with anatomical proton MR images and skull-stripping was performed using a combination of the software packages of AMIDE [61] and MRIcro [62]. The registration process used both the magnet system's table position which was accurate to within ±1mm followed by internal image landmarks such as the sodium calibration standards and the eyeballs. Figure 5.3 presents six different images of the same corresponding coronal section showing the stroke region in the most inferior portion of the right hemisphere. Figure 5.3 shows (top left) the anatomical proton SPGR data by itself for reference (grayscale), (top middle) a skull-stripped SQ sodium image (blue-to-white colorbar shown) acquired after 4 hours of ischemia overlayed on the proton image, (top right) the before reperfusion TSC slope map calculated from 25 sodium images (blue-to orange colorbar shown) overlayed on the proton image, (bottom left) the MAP2 immunostained histological section (see Chapter 4 for a description of MAP2 immunostaining) showing the infarct region indicated by decreased MAP2 immunostaining, (bottom middle) this same MAP2 immunostained section in AMIDE overlayed on the proton image, and (bottom right) the before reperfusion TSC slope map overlayed on both the MAP2 immunostained section in AMIDE and the proton image. Figure 5.3 shows the agreement between the sodium MRI region with the highest rate of TSC increase and the infarct region demonstrated histologically by MAP2 immunostaining.

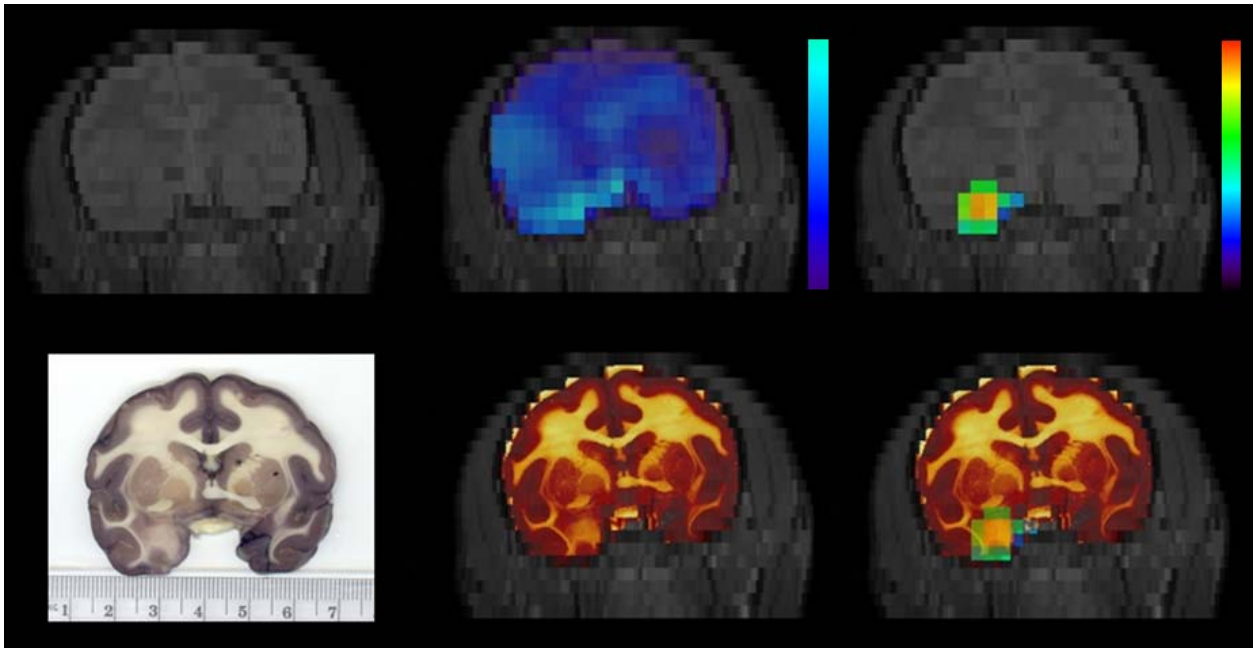

**Figure 5.3: Coronal Images Comparing Stroke in SQ sodium, TSC Slope Map, and MAP2 (top left) The anatomical proton SPGR coronal section by itself for reference (grayscale), (top middle) a skull-stripped SQ sodium coronal image (blue-to-white colorbar) acquired after 4 hours of ischemia overlayed on the proton image, (top right) the before reperfusion TSC rate map calculated from 25 sodium images (blue-to orange colorbar) overlayed on the proton image, (bottom left) the MAP2 immunostained histological section showing the decreased MAP2 immunostaining in the infarct region, (bottom middle) this same MAP2 immunostained section in AMIDE overlayed on the proton image, and (bottom right) the before reperfusion TSC rate map overlayed on both the MAP2 immunostained section in AMIDE and the proton image.**

Linear regression statistical analyses of the time courses of TSC in the ischemic brain (ROI indicated by the TSC rate map) and normal brain were performed in all four animals (see Table 5.1). As expected, in the normal brain (contralateral hemisphere) the TSC slope was not statistically different from zero during MCA occlusion nor after reperfusion in all four animals. The TSC in the ischemic brain (as percent of the normal brain TSC) was found to have a statistically significant positive slope in all four animals ($p < 0.0006$). Figure 5.4 shows the TSC data plotted versus the time after stroke onset for animal #2, where the blue circles denote the mean values and the error bars denote ± the standard error. The results of the linear regression analysis showed a statistically significant increase ($p = 5.20 \times 10^{-8}$) in ischemic brain TSC of 7.15%/hr. As shown in Figure 5.4, the linear regression of the data can be extrapolated to estimate the stroke onset time and this time can be compared to the actual stroke onset time. The time at which the linear regression of the ischemic brain TSC crosses 100% of normal is considered the error in the estimated stroke onset time (0.449hrs for animal #2).

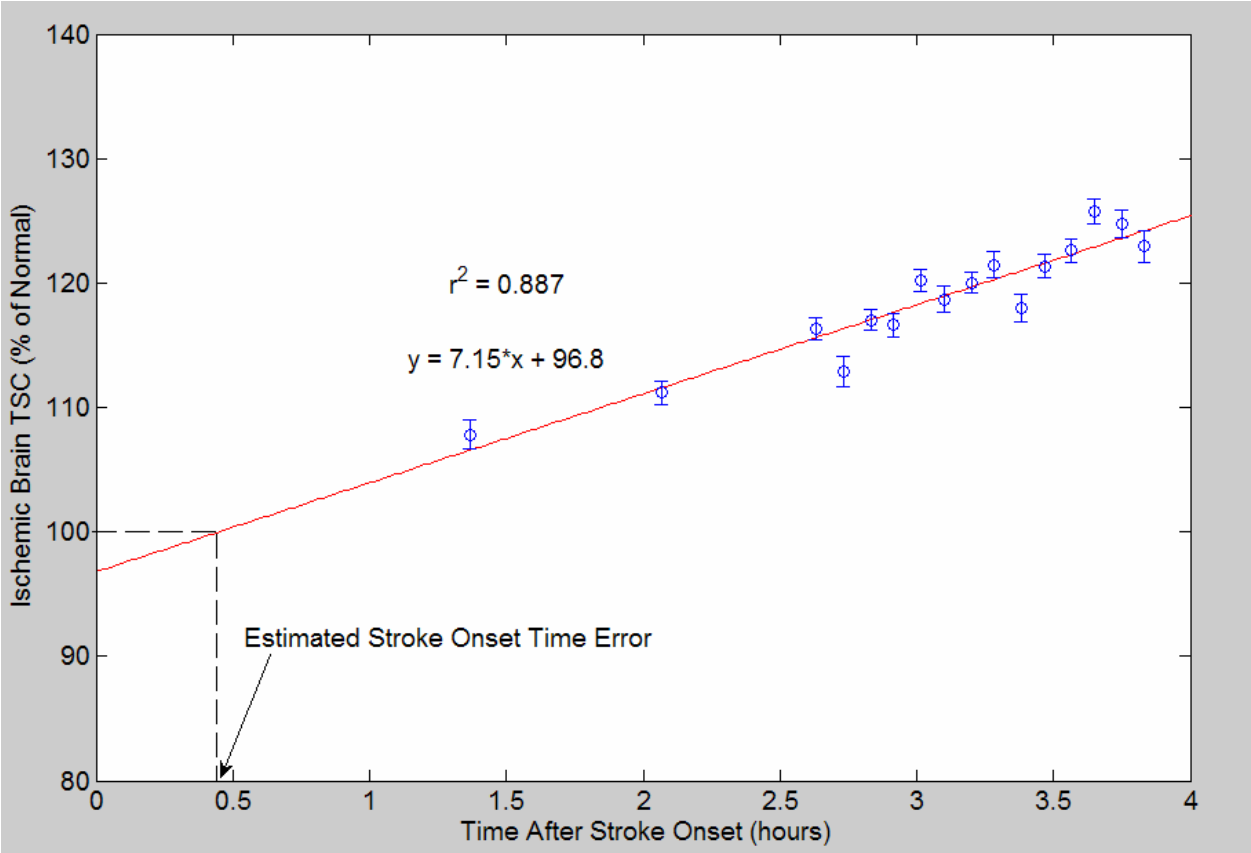


**Figure 5.4: Plot of TSC Data Plotted Versus Time After Stroke Onset for Animal #2**

**Plot of TSC in the ischemic brain (as % of the normal brain TSC) plotted versus time after stroke onset for animal #2 (blue circles denote mean values and the error bars denote ± standard error). The results of the linear regression analysis (red line) showed a statistically significant increase ($p = 5.20 \times 10^{-8}$) in ischemic brain TSC of 7.15%/hr. The time at which the linear regression of the ischemic brain TSC crosses 100% of normal is the error in the estimated stroke onset time (0.449hrs for animal #2).**

**Table 5.1: Rate of Brain Tissue Sodium Concentration Increase During MCA Occlusion**

| Animal # | # of Sodium Images | Rate of TSC Increase During MCA Occlusion (%/hr ± 95% Confidence Interval) | | | Error in Estimated Stroke Onset Time (hrs) |
|---|---|---|---|---|---|
| | | Normal Brain | Ischemic Brain | p-value | |
| 1 | 25 | 0.52 ± 1.52 | 5.85 ± 1.97 | $3.00 \times 10^{-7}$ | -0.235 |
| 2 | 16 | -1.08 ± 1.20 | 7.15 ± 1.46 | $5.20 \times 10^{-8}$ | 0.449 |
| 3 | 17 | -1.28 ± 1.67 | 6.99 ± 3.41 | $5.53 \times 10^{-4}$ | -0.168 |
| 4 | 24 | 0.41 ± 2.29 | 5.44 ± 2.34 | $7.93 \times 10^{-5}$ | 0.317 |

Figure 5.5 shows the TSC data plotted versus the time after stroke onset for all four animals, where the circles denote the mean values and the error bars denote ± the standard error. For animal #1 (blue), the TSC in the ischemic brain was found to have a statistically significant positive slope of 5.85%/hr with a p-value of $3.00 \times 10^{-7}$, and the linear regression estimated the stroke onset time with an error of -0.235hrs. For animal #2 (green), the TSC in the ischemic brain was found to have a statistically significant positive slope of 7.15%/hr with a p-value of $5.20 \times 10^{-8}$, and the linear regression estimated the stroke onset time with an error of 0.449hrs. For animal #3 (red), the TSC in the ischemic brain was found to have a statistically significant positive slope of 6.99%/hr with a p-value of $5.53 \times 10^{-4}$, and the linear regression estimated the stroke onset time with an error of -0.168hrs. For animal #4 (black), the TSC in the ischemic brain was found to have a statistically significant positive slope of 5.44%/hr with a p-value of $7.93 \times 10^{-5}$, and the linear regression estimated the stroke onset time with an error of 0.317hrs.

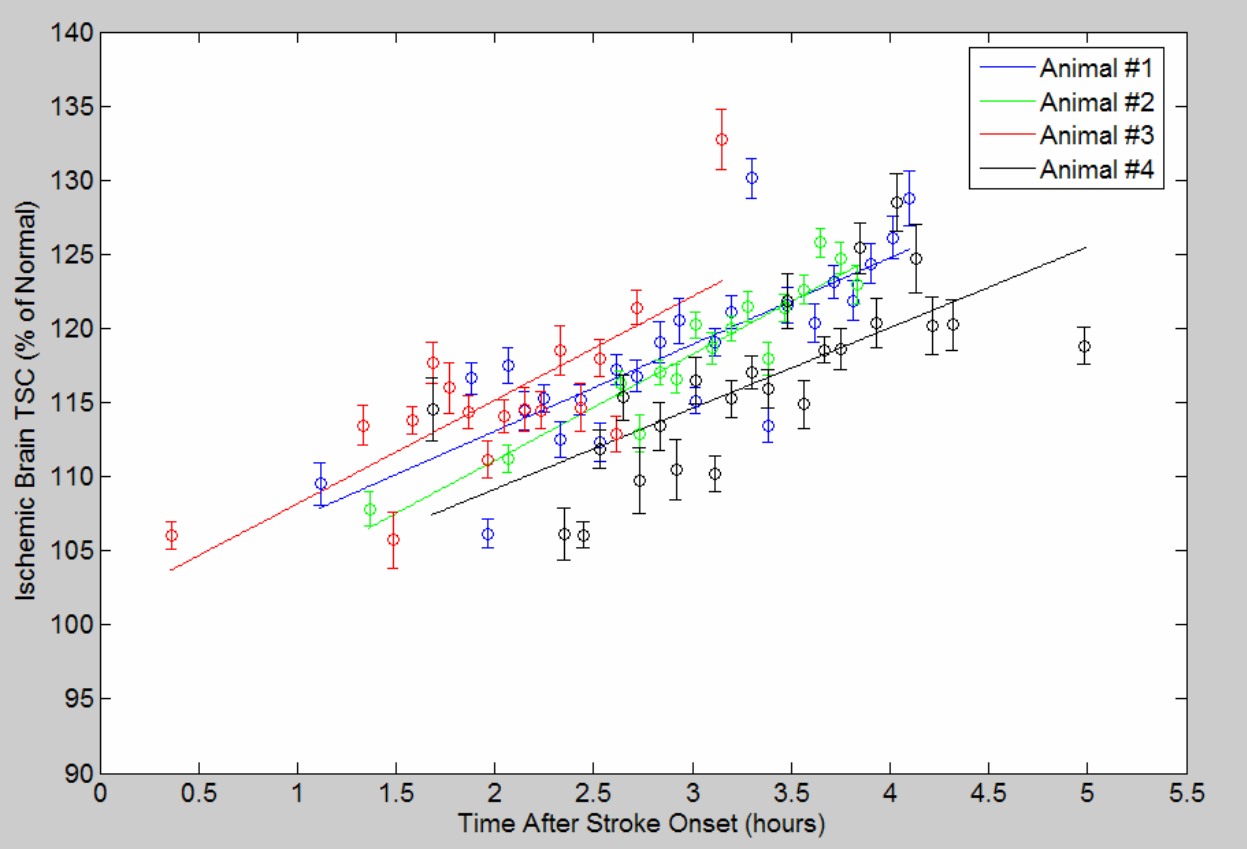


**Figure 5.5: Plot of Ischemic Brain TSC Slopes for the Four Non-Human Primates**

**TSC data plotted versus time after stroke onset for all four animals (circles denote mean values and the error bars denote ± standard error). The results of the linear regression analyses which found statistically significant positive slopes in all four animals are also shown. The TSC slope was 5.85%/hr ($p = 3.00 \times 10^{-7}$) for animal #1 (blue), with an error of -0.235hrs in the estimated stroke onset time. The TSC slope was 7.15%/hr ($p = 5.20 \times 10^{-8}$) for animal #2 (green), with an error of 0.449hrs in the estimated stroke onset time. The TSC slope was 6.99%/hr ($p = 5.53 \times 10^{-4}$) for animal #3 (red), with an error of -0.168hrs in the estimated stroke onset time. The TSC slope was 5.44%/hr ($p = 7.93 \times 10^{-5}$) for animal #4 (black), with an error of 0.317hrs in the estimated stroke onset time.**

The existence of a stroke/infarct created by the endovascular occlusion was verified histologically in all four animals using immunohistochemical staining with antibodies to microtubule associated protein 2 (MAP2). Chapter 4 gives a detailed description of the thick tissue section MAP2 immunostaining protocol, and how it allows the identification of the infarct region by the decreased MAP2 immunostaining that occurs there. In all four animals, decreased MAP2 immunostaining (indicating infarction) was seen in the region indicated by the sodium MRI TSC rate maps as having statistically significant TSC slopes. This is demonstrated for animal #1 in the bottom row of Figure 5.3.

Deflation and removal of the balloon catheter in the right MCA was performed at 5.2hrs after stroke onset in animal #1, at 4.1hrs after stroke onset in animal #2, at 3.5hrs after stroke onset in animal #3, and at 5.4hrs after stroke onset in animal #4. After deflation and removal of the balloon catheter, 25, 18, 20, and 20 sodium images were acquired in animals #1-4, respectively. Linear regression statistical analyses of the time courses of TSC in the ischemic brain and normal brain after the deflation and removal of the balloon catheter were performed in all four animals. As expected, in the normal brain (contralateral hemisphere) the TSC slope was not statistically different from zero after the deflation and removal of the balloon catheter in all four animals. In animals #1, #3, and #4, proton MR angiography verified that the deflation and removal of the balloon catheter in the right MCA resulted in the reperfusion of blood flow to that artery. Linear regression statistical analyses of the time courses of ischemic brain TSC after reperfusion of the MCA in animals #1, #3, and #4 resulted in TSC slopes that were not statistically different from zero in these three animals. In fact, in each of these three animals there was a statistically significant change from a positive TSC slope during MCA occlusion to a TSC slope after MCA reperfusion that was not statistically different from zero. In animal #2,

proton MR angiography verified that the deflation and removal of the balloon catheter in the right MCA resulted in almost no reperfusion of blood flow to that artery. Thus, after deflation and removal of the balloon catheter with almost no reperfusion of blood flow to the right MCA in animal #2, the TSC in the ischemic brain was found to have a statistically significant positive slope of 5.28±3.44%/hr (± 95% confidence interval) with a p-value of 0.005.

## 5.5 CONCLUSIONS

We demonstrated the use of single quantum (SQ) sodium MRI for measuring the time course of TSC in a non-human primate model of reversible focal brain ischemia. Our results demonstrated that TSC increases slowly and linearly as a function of time after the onset focal brain ischemia. Decreased MAP2 immunostaining indicating infarction was seen in the region indicated by the sodium MRI TSC rate maps as having statistically significant TSC slopes. There was a statistically significant change from a positive TSC slope during MCA occlusion to a TSC slope after MCA reperfusion that was not statistically different from zero. In addition, the rate of the TSC increase in ischemia was found to be spatially heterogeneous with a spatial distribution that changes upon tissue reperfusion and that cannot be explained through partial voluming effects. This hetereogeneity may have potential applications for assessing tissue viability in acute stroke. Finally, our results indicate that sodium MRI could predict the stroke onset time in patients that are unsure when their symptoms began, potentially extending the use of tPA therapy to patients that would otherwise not receive treatment.

# 6.0 SERIAL TRIPLE QUANTUM SODIUM MRI DURING NON-HUMAN PRIMATE FOCAL BRAIN ISCHEMIA

## 6.1 ABSTRACT

Triple quantum (TQ) sodium MR imaging techniques with clinically acceptable 18 minute data acquisition times are demonstrated *in vivo* in a non-human primate model of focal brain ischemia. Focal brain ischemia was induced in four animals using embolization coils to occlude the posterior cerebral artery and a balloon catheter to occlude the middle cerebral artery. A statistically significant increase ($p < 0.001$) in the TQ sodium MRI signal intensity in the ischemic hemisphere relative to the contralateral hemisphere was seen at all time points in all four animals. This increased TQ sodium MRI signal intensity was demonstrated as early as 34 minutes after the onset of ischemia. The TQ sodium MRI hyperintensity corresponded to the anatomical location of the ischemic cortex as indicated by the registration of the TQ image data with anatomical proton MR image data. The results demonstrated that early after the onset of ischemia, there was an increase in the TQ signal intensity in the ischemic hemisphere with negligible change in the single quantum (SQ) signal intensity.

## 6.2 INTRODUCTION

Stroke is the third largest cause of mortality in the United States. In addition, stroke accounts for a significant portion of the country's health care expenditures because of the severe disabilities and long recovery periods that stroke survivors experience. Normal brain cells maintain a large sodium ion concentration gradient across their membrane, with an intracellular sodium concentration of about 20mM and an extracellular sodium concentration of about 140mM [15]. This sodium concentration gradient is essential to many of the basic physiological functions of the cell [14]. The gradient is maintained by sodium-potassium-ATPase (Na-K-ATPase), an ion pump that splits ATP (adenosine tri-phosphate) to pump $Na^+$ out of the cell and $K^+$ into the cell. ATP is the cell's primary energy currency, and, under normal physiological conditions, the maintenance of the large sodium concentration gradient by Na-K-ATPase requires a large proportion of the cell's ATP [16, 19, 24].

Ischemia such as that in acute stroke causes abnormal or impaired energy metabolism and, thus, disturbs the Na-K-ATPase, which in turn interrupts the continuous pumping of sodium out of the cell [16]. The result is that very quickly after the onset of ischemia, there is an increase in the intracellular sodium concentration (ISC) due to a redistribution of sodium ions from the extracellular compartment to the intracellular compartment with no net change in the total tissue sodium concentration. Gradually, the total tissue sodium concentration (TSC) also increases in ischemia [23, 34-42]. Although both ISC and TSC increase in ischemia, the increase in ISC occurs earlier. Therefore, a non-invasive method for detecting this early physiological change could be an invaluable tool for the diagnosis and study of acute stroke.

Currently, there are two well-accepted methods used for separating the intracellular sodium and extracellular sodium nuclear magnetic resonance (NMR) signals [24]. The first method for separating these signals uses an exogenously administered shift reagent to which the cell membrane is impermeable. A shift reagent (SR) is a negatively charged paramagnetic compound that forms complexes with biological cations, thereby altering the magnetic field that the cations experience and shifting their resonance frequency [14, 15]. The disadvantages with the use of SR's are their toxicity and the somewhat invasive nature of the injection or infusion of SR's [14, 15]. Because the cell membrane is impermeable to the SR, only the resonant frequency of the extracellular sodium is shifted, allowing for the separation of the sodium NMR signals from the intracellular and extracellular compartments [14, 15]. In addition to the toxicity of SR's, which prohibits their use in humans, the fact that SR's do not cross the blood brain barrier makes their use for studying the brain difficult even in animal models. Consequently, the separation of the intra- and extracellular sodium content in the brain using shift reagents, although possible using hyperosmotic mannitol to break the blood brain barrier [30], is not an attractive means for the study of impaired ion homeostasis during ischemia.

The second method for separating the intracellular sodium and extracellular sodium NMR signals is to use relaxation-based techniques, such as multiple-quantum (MQ) filtering, that take advantage of the different transverse relaxation properties that the sodium nucleus exhibits in the intracellular and extracellular compartments. Several reports have demonstrated that the MQ sodium NMR signal from biological tissue comes primarily from the sodium in the intracellular space [14, 15, 25-30], as opposed to the total tissue sodium content as measured in total (single quantum) sodium MRI. This feature of MQ filtering techniques has been used to study changes in intracellular sodium concentration (ISC) in a variety of tissues using NMR

spectroscopy [14, 15, 25-30]. Lyon et al. [27] performed experiments in which they acquired double quantum (DQ) sodium NMR spectra of the rat brain both before and after the rat was killed with an overdose of sodium pentobarbital. Lyon et al. [27] saw increases as large as about 800% in the DQ sodium NMR spectra in the rat brain after death. Imaging extensions of these MQ sodium NMR techniques in animals have also been demonstrated [31]. Kalyanapuram et al. [31] obtained 3D TQ sodium MR images of the dog brain *in vivo* with data acquisition times of 105 minutes. In Kalyanapuram et al.'s [31] experiments, TQ images were acquired both before and after the animal was killed with an overdose of sodium pentobarbital. They saw a 40-50% increase in the TQ sodium MRI signal intensity in the dog brain after death. These imaging extensions of these MQ techniques have been less common because of the weak nature of the MQ sodium NMR signal. Recently, though, efficient imaging schemes have allowed the acquisition of TQ sodium MR images in the *in vivo* human brain in clinically acceptable data acquisition times [16]. Consequently, TQ sodium MRI may prove to be useful for the non-invasive visualization of the increase in ISC that occurs in brain ischemia and the study of its role on the determination of tissue viability before reperfusion. In this paper, we demonstrate TQ sodium MRI in a non-human primate model of focal brain ischemia, in which the animal is alive as opposed to dead [27, 31] during the TQ sodium MR of the evolving brain ischemia.

## 6.3 METHODS

### 6.3.1 Animal Preparation

Under a protocol approved by the Institutional Animal Care and Use Committee (IACUC), focal brain ischemia was induced in pig-tail monkeys (*Maccaca nemestrina*, n=4) using the endovascular model described in detail in Chapter 2 of this thesis. Using this model, ischemia was achieved using embolization coils to occlude the posterior cerebral artery (PCA) and a balloon catheter to occlude the middle cerebral artery (MCA) on the right hemisphere of the animals (Figure 6.1a).

### 6.3.2 MR Imaging

The *in vi*vo MRI studies were performed on the MRRC's 3 Tesla whole body scanner (General Electric Medical Systems, Milwaukee, WI) using $^{23}$Na and $^{1}$H quadrature birdcage RF coils custom-built to fit the animal's head (AIRI, Cleveland, OH). Proton time of flight magnetic resonance angiography (MRA) scans (FOV = 16cm, TE = 4.7ms, TR = 35ms, $\theta = 25°$) were performed to verify that both the PCA and MCA on the animal's right hemisphere were still occluded after the transfer of the animal from the angiography suite. Anatomical proton 3D spoiled gradient recalled (SPGR) images were also acquired for registration purposes (FOV = 16cm, TE = 15ms, TR = 35ms, $\theta = 25°$). Three-dimensional triple quantum (TQ) sodium MR imaging was performed at different time points during the experiment. The TQ sodium images were acquired using a modification of a twisted projection imaging (TPI) sequence [19] that implemented a three-pulse triple quantum coherence transfer filter, as presented by Hancu et al. [16], with a preparation time of 3.0ms. The k-space encoding used a 214 shot TPI trajectory,

leading to a time of 26 seconds per full k-space volume (TR = 120ms). The six-phase TQ selective filter was repeated 7 times for each shot, resulting in a total scan time of 18 minutes. In addition to the TQ imaging, 3D single quantum (SQ) sodium MR images were acquired using TPI (816 scans, TE = 0.5ms, TR = 100ms, and NEX = 4 for a total SQ scan time of 5.5 minutes). The reconstructed TQ and SQ sodium images were obtained by using a regridding algorithm (tri-linear kernel, window width one, no oversampling), producing a 64x64x64 stack for each image. For both the TQ and SQ imaging, the field of view (FOV) was 20x20x20cm, resulting in a voxel size or resolution of 3.125x3.125x3.125mm.

## 6.4 RESULTS AND DISCUSSION

The effectiveness of this model is shown in Figure 6.1b, where a proton MR angiogram (MRA) from a representative animal acquired after the endovascular occlusion of the right PCA and MCA is presented. The MRA clearly demonstrates blood flow in the MCA and PCA on the left side, but not on the right side of the brain.

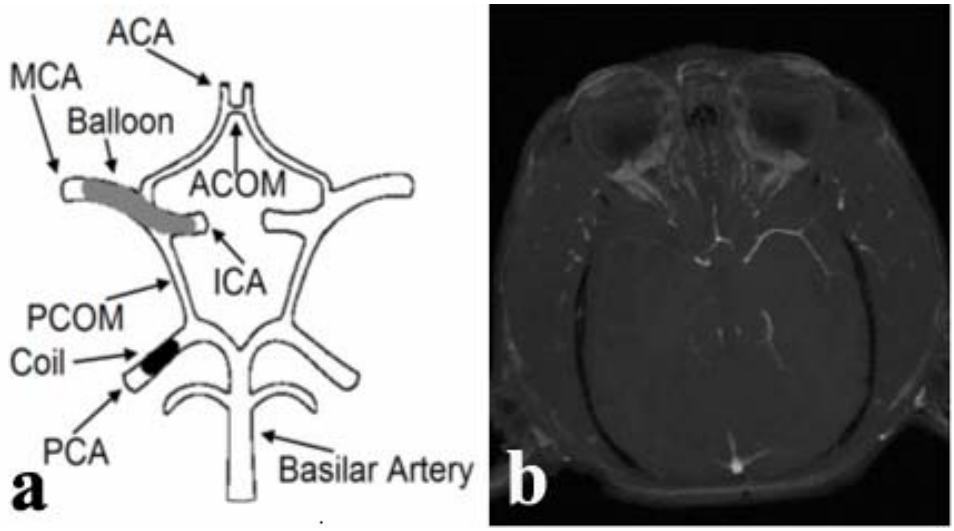


**Figure 6.1: Proton MRA of Right MCA and PCA Occlusion for TQ Image Comparison**
**(a) Schematic diagram of the inferior view of the cerebral vasculature after endovascular occlusion, showing the positions of the balloon catheter (gray cylinder) in the right MCA and embolization coils (dark cylinder) in the right PCA. (b) Proton MRA acquired after endovascular occlusion of the right PCA and MCA. The MRA clearly demonstrates blood flow in the MCA and PCA on the left side of the brain, but no blood flow in both the right MCA and right PCA.**

Figure 6.2 shows selected partitions from three TQ sodium MR images acquired at 34 minutes = 0.57 hours (a, top row), 169 minutes = 2.82 hours (b, middle row), and 353 minutes = 5.83 hours (c, bottom row) after the endovascular occlusion. (Note that the balloon catheter in the right MCA was deflated and removed 3.5 hours after the endovascular occlusion, resulting in partial reperfusion of the right MCA; therefore, the TQ image at the 5.83 hour time point was acquired 2.35 hours after this event.) The TQ images were calibrated using sodium calibration standards within the image field of view (40mM, 80mM, and 120mM NaCl in 10% agarose). The results show increased TQ sodium MRI intensity on the right side of the brain compared to the left side of the brain already at 34 minutes after the endovascular occlusion, but also at 2.82 hours and 5.83 hours.

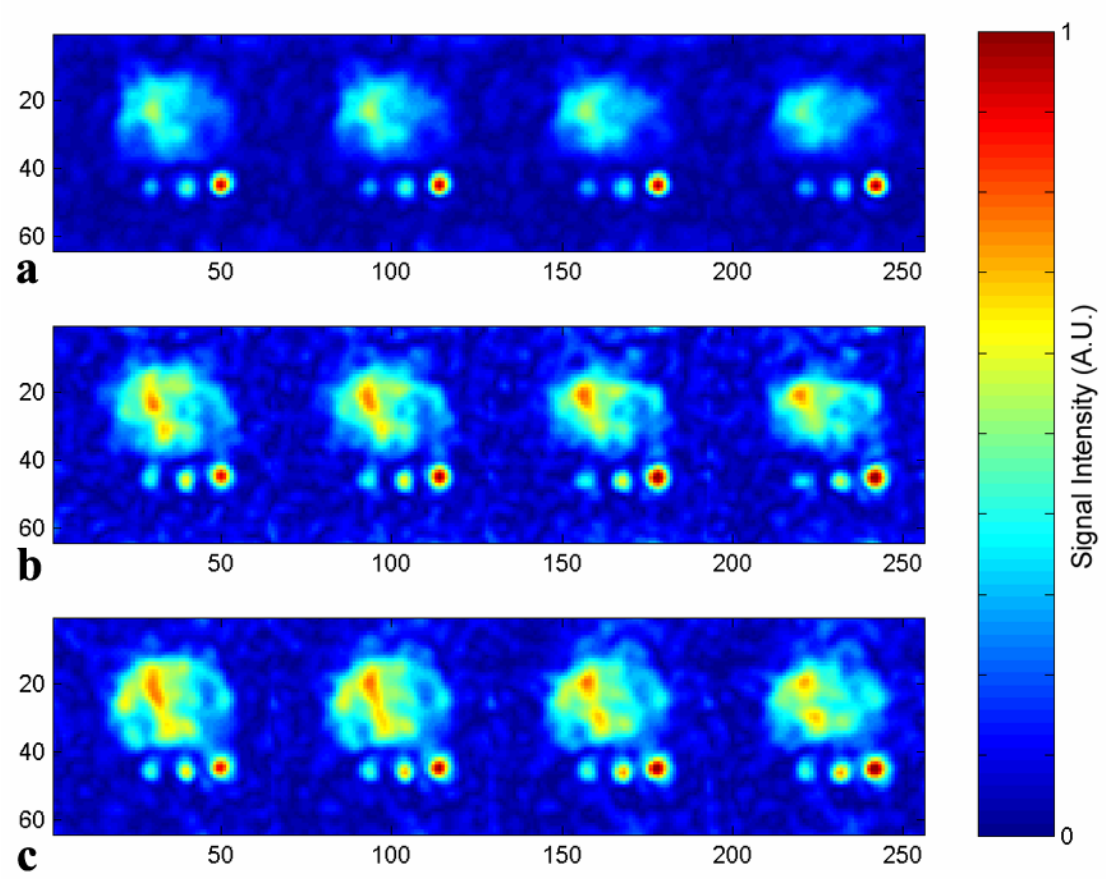


**Figure 6.2: 3D TQ Sodium MR Images Acquired at Several Time Points After Ischemia**
**Selected partitions from 3D TQ sodium MR images acquired at 34 minutes = 0.57 hours (a, top row), 169 minutes = 2.82 hours (b, middle row), and 353 minutes = 5.83 hours (c, bottom row) after the endovascular occlusion. The colormap used for displaying the images is shown to the right of the figure. Increased TQ sodium MRI signal intensity on the right side of the brain compared to the left side of the brain is seen at all three time points.**

Figure 6.3 shows the corresponding SQ sodium MRI results which represent the total tissue sodium concentration within the voxel. Figure 6.3 shows the corresponding selected partitions from three SQ sodium MR images acquired at 22 minutes = 0.37 hours (a, top row), 163 minutes = 2.72 hours (b, middle row), and 347 minutes = 5.78 hours (c, bottom row) after the endovascular occlusion. These results demonstrate that at the early time point (a, top row) there is almost no change in the SQ sodium MRI signal intensity on the right hemisphere relative to contralateral. This SQ result sharply contrasts the increased TQ sodium MRI signal intensity on the right side of the brain compared to the left demonstrated at the early time point in the top row (a) of Figure 6.2.

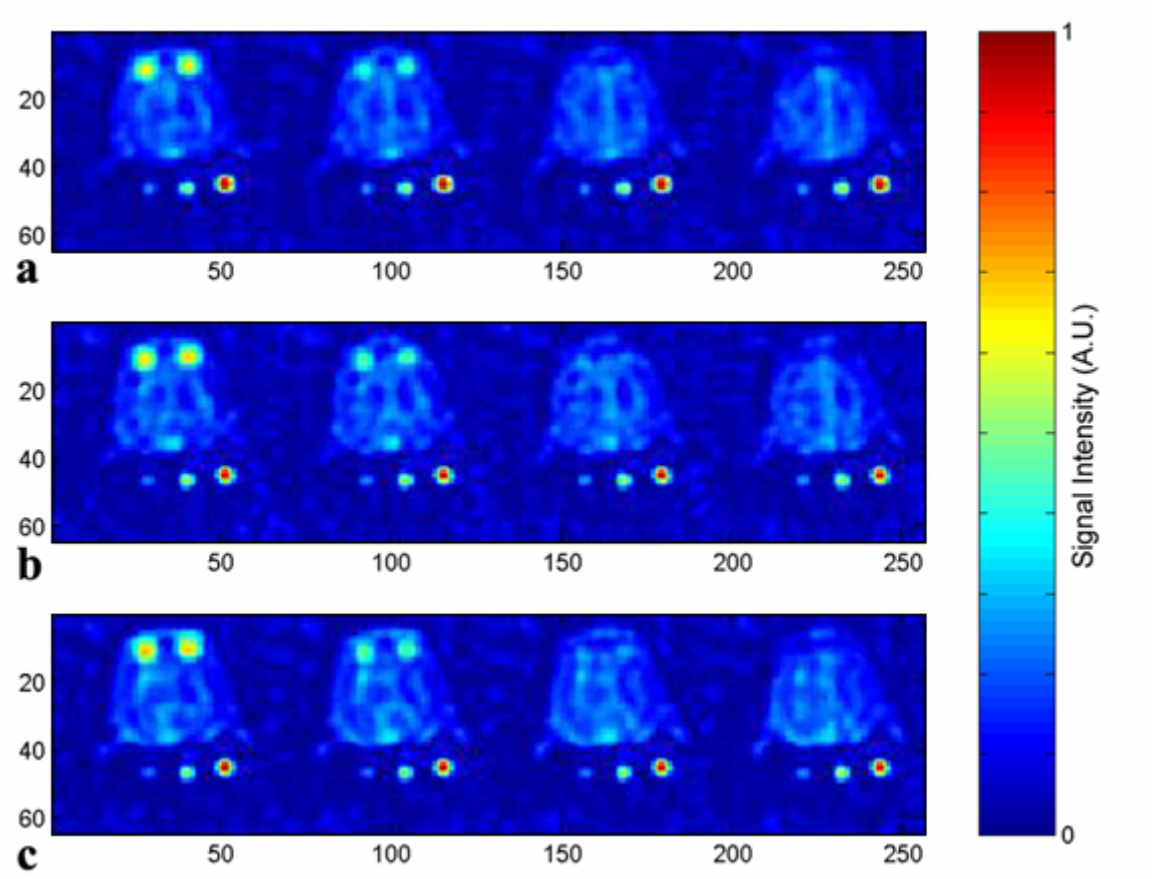


**Figure 6.3: 3D SQ Sodium MR Images for Comparison with TQ Images in Figure 6.2**
**Selected partitions from 3D SQ sodium MR images acquired at 22 minutes = 0.37 hours (a, top row), 163 minutes = 2.72 hours (b, middle row), and 347 minutes = 5.78 hours (c, bottom row) after the endovascular occlusion. The colormap used for displaying the images is shown to the right of the figure. Almost no change in the SQ sodium MRI signal intensity on the right side of the brain compared to the left side of the brain is seen at the early time point.**

In order to demonstrate the specific brain location of the TQ hyperintensity, registration of the TQ images with anatomical proton MR images and skull-stripping was performed using a combination of the medical image analysis software packages of AMIDE [61] and MRIcro [62]. The registration process used both the magnet system's table position which was accurate to within ±1mm followed by landmarks within the images such as the sodium calibration standards and the eyeballs. (The animal's head and the sodium calibration standards are all immobilized together as a unit on the custom-built table and do not move with respect to each other throughout the experiment.) Figure 6.4 presents skull-stripped axial (left), coronal (middle), and sagittal (right) sections through the hyperintense region in the right MCA territory of the brain for the TQ sodium image obtained at the 2.82 hour time point (color) registered with the proton SPGR data set (grayscale). This again shows increased TQ intensity on the right side of the brain compared to the left at 2.82 hours after endovascular occlusion. There are two regions of increased signal intensity (see the axial section) in this TQ image which lie mostly within the right MCA and right PCA territories, respectively, and will be referred to as the MCA and PCA regions of interest (ROI's).

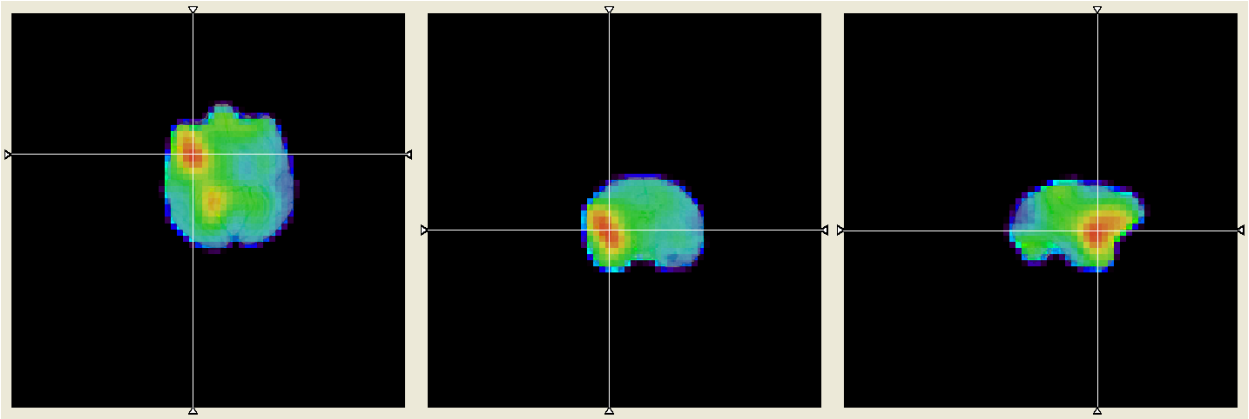

**Figure 6.4: Axial, Coronal, and Sagittal Sections of TQ Hyperintensity in Ischemic Brain Skull-stripped axial (left), coronal (middle), and sagittal (right) sections through the hyperintense region in the right MCA territory for the 2.82 hour time point TQ sodium image (color) registered with an anatomical proton MR data set (grayscale). The white "cross hairs" on each section indicate the relative location of the other two perpendicular sections.**

Figure 6.5 shows a plot of the relative increase in TQ sodium MRI signal intensity on the right side of the brain (as % of contralateral baseline signal intensity, where 100% is no increase) for these two ROI's at the three different time points. Both the MCA and PCA ROI signal intensities were greater than the contralateral signal intensity at all time points with a statistical significance of $p < 0.001$ (student's t-test). At each individual time point, the relative increase for the MCA ROI was greater than that for the PCA ROI with a statistical significance of $p < 0.005$. For the MCA ROI, there was a statistically significant increase ($p < 0.005$) in the TQ relative change from the 0.57 hour time point to the 2.82 hour time point, and then a statistically significant decrease ($p < 0.005$) from the 2.82 hour time point to the 5.83 hour time point (which was 2.35 hours after partial reperfusion of the right MCA). For the PCA ROI, there was a statistically significant increase ($p < 0.005$) in the TQ relative change from the 0.57 hour time

point to the 2.82 hour time point, but then there was no statistically significant decrease even at the $p < 0.10$ level from the 2.82 hour time point to the 5.83 hour time point (which was 2.35 hours after partial reperfusion of the right MCA). Thus, after partial reperfusion of the right MCA, there was a statistically significant decrease in the TQ relative increase for the MCA ROI, but not for the PCA ROI.

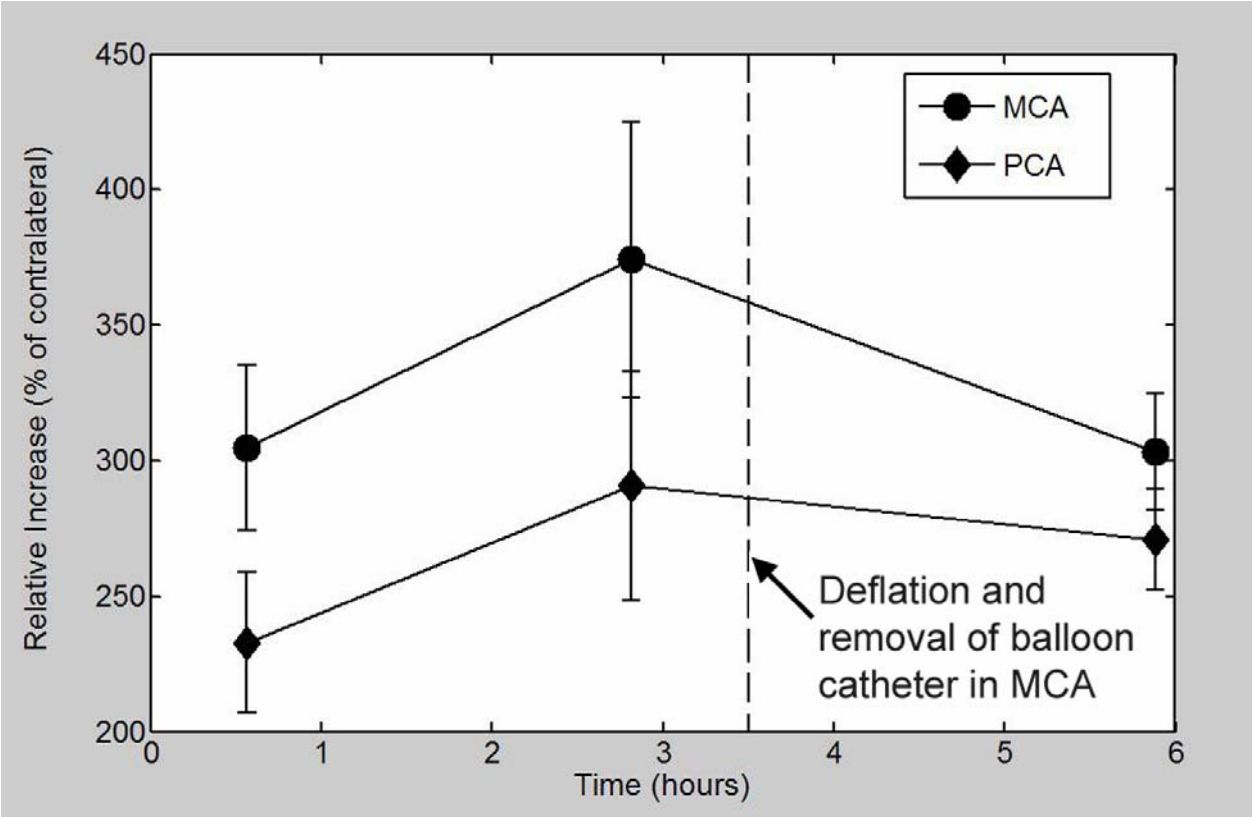


**Figure 6.5: Plot of Relative Increase in TQ Sodium MRI Intensity in Ischemic Hemisphere** Plot of the relative increase in TQ sodium MRI signal intensity on the right side of the brain (as % of contralateral baseline signal intensity, where 100% is no increase) for the ROI's in the right MCA and right PCA territories. The points denote mean values and the error bars denote ± one standard deviation. Both the MCA and PCA ROI signal intensities were greater than the contralateral signal intensity at all time points with a statistical significance of $p < 0.001$ (student's t-test). At each individual time point, the relative increase for the MCA ROI was greater than that for the PCA ROI with a statistical significance of $p < 0.005$. For both ROI's, there was a statistically significant increase ($p < 0.005$) in the TQ relative change from the 0.57 hour time point to the 2.82 hour time point. However, after partial reperfusion of the right MCA, there was a statistically significant decrease in the TQ relative increase for the MCA ROI ($p < 0.005$), but not for the PCA ROI (even at the $p < 0.10$ level).

A statistically significant increase ($p < 0.001$) in the TQ sodium MRI signal intensity in the ischemic hemisphere relative to the contralateral hemisphere was seen at all time points in all four animals. Three of the four animals had TQ images done at similar early time points. Averaging these three early time points from the different animals gave a relative increase (as % of contralateral baseline signal intensity, where 100% is no increase) in the MCA region of 226.32$\pm$69.85% (mean $\pm$ standard deviation) at a time after occlusion of 0.85$\pm$0.42 hours (mean $\pm$ standard deviation). A different three of the four animals had TQ images done at similar middle time points. Averaging these three middle time points from the different animals gave a relative increase in the MCA region of 275.13$\pm$91.04% at a time after occlusion of 2.70$\pm$0.31 hours. In only two of the four monkeys were TQ scans performed after deflation and removal of the balloon catheter to achieve reperfusion in the right MCA. Averaging these two late time points (one 2.35 hours after reperfusion, the other 2.20 hours after reperfusion) gave a relative increase in the MCA region of 264.92$\pm$54.21% at a time after occlusion of 6.09$\pm$0.29 hours.

## 6.5 CONCLUSIONS

Triple quantum 3D sodium MR images obtained with clinically acceptable 18 minute data acquisition times have been demonstrated *in vivo* in a non-human primate model of focal brain ischemia. Increased TQ sodium MRI signal intensity was demonstrated in the ischemic hemisphere relative to the contralateral hemisphere as early as 34 minutes after the onset of ischemia. The results demonstrated that early after the onset of ischemia, there was a sharp increase in the TQ signal intensity with almost no change in the SQ signal intensity. This could be attributed to either an increase in the intracellular sodium concentration due to a redistribution

of sodium ions within the voxel following the failure of the Na-K-ATPase, or just a change in the relaxation rates. Acute ischemia, however, is not likely to create fast and reversible changes in the tissue's transverse relaxation rates that could be reversed upon reperfusion. Thus, the increase in the TQ sodium MRI signal intensity observed in the ischemic hemisphere is hypothesized to be largely due to an increase in the intracellular sodium concentration (ISC) as a result of impaired ion homeostasis during evolving brain ischemia. The quantification of this fast change in ISC could be used in combination with measures of TSC to help distinguish between non-viable and viable tissue. Our results are supportive of this hypothesis, but more studies will be required to completely validate its use.

# 7.0 CONTRIBUTION OF THE EXTRACELLULAR SODIUM POOL TO THE BRAIN'S TRIPLE QUANTUM SODIUM MR SIGNAL

## 7.1 ABSTRACT

This study investigated the contribution of the extracellular sodium pool to the brain's triple quantum (TQ) sodium MR signal. The extracellular sodium MR signal was separated from the intracellular sodium MR signal in the *in vivo* rat brain using the thulium shift reagent, $TmDOTP^{5-}$, which does not cross the cell membrane [14, 15]. In order to get the shift reagent (SR) across the blood brain barrier (BBB), hyperosmotic mannitol was used to break the BBB [63, 64]. Single quantum (SQ) and TQ sodium MR spectra were acquired both before (control spectra) and after (experimental spectra) the administration of mannitol and $TmDOTP^{5-}$ into the common carotid arteries. The results showed that within the SNR of the experiment there was no evidence of any TQ sodium MR signal from the brain's extracellular sodium pool (i.e. at the 2-6kHz frequency offset of the SR-shifted extracellular space).

## 7.2 INTRODUCTION

Ischemia such as that in acute stroke causes abnormal or impaired energy metabolism and, thus, disturbs the sodium-potassium-ATPase, interrupting the continuous pumping of sodium out of the cell. The result is an increasing intracellular sodium concentration (ISC) in focal brain ischemia. In addition to the increase in ISC, the total tissue sodium concentration (TSC) also increases in ischemia [23, 34-42]. Although both ISC and TSC increase in ischemia, the increase in ISC is more sensitive; therefore, a non-invasive method for monitoring brain ISC would be a valuable diagnostic tool in acute stroke. In other words, a way to non-invasively separate out the intracellular sodium concentration from the extracellular sodium concentration could be clinically important.

Currently, there are two well-accepted methods used for separating the intracellular sodium and extracellular sodium nuclear magnetic resonance (NMR) signals [24]. The first method for separating these signals uses an exogenously administered shift reagent to which the cell membrane is impermeable. A shift reagent (SR) is a negatively charged paramagnetic compound that forms complexes with biological cations, thereby altering the magnetic field that the cations experience and shifting their resonance frequency [14, 15]. The disadvantages with the use of SR's are their toxicity, which prevents their use in humans, and the somewhat invasive nature of the injection or infusion of SR's [14, 15]. The shift reagent used in this study is $TmDOTP^{5-}$, or thulium-1,4,7,10-tetraacacyclododecane-1,4,7,10-tetra methylene phosphonate. Because the SR does not cross the cell membrane, it only shifts the resonance frequency of the extracellular sodium, allowing for the separation of the sodium NMR signals from the intracellular and extracellular compartments [14, 15].

The second method for separating the intracellular sodium and extracellular sodium NMR signals is to use relaxation-based techniques, such as multiple-quantum (MQ) filtering, that take advantage of the different transverse relaxation properties that the sodium nucleus exhibits in the intracellular and extracellular compartments. Several reports have demonstrated that the MQ sodium NMR signal from biological tissue arises primarily from the sodium in the intracellular space [14, 15, 25-30]. In fact, SR's have been used in conjunction with TQ sodium NMR for investigating the very large contribution of the intracellular sodium to the TQ sodium NMR signal in the rat liver [15], rat kidney [14], and rat heart [25]. However, this has not been done in the brain because SR's do not cross the blood brain barrier (BBB). We propose that breaking the BBB to allow the SR into the brain could allow the investigation of the extracellular sodium pool's contribution to the TQ sodium NMR signal in the brain. Hyperosmotic mannitol has been shown as a successful technique for breaking the BBB [63, 64]. In this study, hyperosmotic mannitol is used to break the BBB, so that the SR, $TmDOTP^{5-}$, can cross the BBB and separate the sodium NMR signals from the intracellular and extracellular compartments in the *in vivo* rat brain.

## 7.3 METHODS

Under a protocol approved by the Institutional Animal Care and Use Committee (IACUC), thirty-two Male Sprague-Dawley rats (~450g) were prepared under inhalation isoflurane (2%), $N_2O$ (30%), and balance $O_2$, administered via endotracheal tube and volume controlled artificial respiration (Model 681, Harvard Apparatus, South Natick, MA). Surgery was performed to cannulate the femoral artery, femoral vein, and both common carotid arteries (CCA's) with PE-

50 polyethylene catheters. The femoral artery cannula was used for the continuous monitoring of arterial blood pressure (BP) using a strain gauge transducer (to monitor the rat's condition and state of anesthesia) during both the surgery and the MR scanning. Body temperature was maintained at 37°C by a servo-controlled heating pad and a rectal thermistor during surgery, and by a thermostatic cradle (with recirculating heated water) during MR scanning. The CCA cannulas were used for the administration of 25% w/v mannitol, and the shift reagent $TmDOTP^{5-}$ (Macrocyclics, Dallas, TX) was administered at a concentration of 80mM. SQ and TQ sodium FID's were acquired on a 3T whole body MRI scanner (General Electric Medical Systems, Milwaukee, WI) using a custom-built, dual-tuned ($^{1}H/^{23}Na$), dual-quadrature, 8-pole, 5cm diameter radiofrequency (RF) birdcage coil [65]. The SQ sodium FID's were acquired with TE = 0.1ms, TR = 100ms, and 2140 averages. The TQ sodium FID's were acquired using a three-pulse triple quantum coherence transfer filter, as presented by Hancu et al. [16], with a preparation time of 5.0msec, TE = 0.1ms, TR = 120ms, and 428 averages.

## 7.4 RESULTS AND DISCUSSION

First, trypan blue experiments were done to determine the time-course, optimal dose, and the more efficient route of administration of the mannitol. Trypan blue is a stain that does not cross the intact BBB [66]. From these trypan blue experiments (n = 8 rats), bolus injection of 25% w/v mannitol into the CCA was determined to be more effective than infusion for breaking the BBB. Figure 7.1 presents a section from a harvested rat brain where administration of a mannitol bolus (3.8mL, 25% w/v) into the right CCA was followed by injection of 0.41% trypan blue solution also into the right CCA. Figure 7.1 shows that the trypan blue (administered after

mannitol) successfully crossed the BBB on the right side of the brain leading to a cerebral-blood-flow-modulated blue staining of the brain parenchyma. Little trypan blue staining is observed in the contralateral hemisphere (some staining occurs there due to circulation through the circle of Willis and late systemic redistribution of the dye). The trypan blue staining demonstrated in Figure 7.1 was not observed with the administration of mannitol at the same concentration into the femoral vein (all body organs except the brain were stained with trypan blue in that case). Figure 7.1 also illustrates that a heterogeneous distribution of the SR is expected; therefore, the linewidth of the SR-shifted peak in the measured spectra will be affected by the ensuing spread of resonant frequencies in the SR-shifted extracellular space.

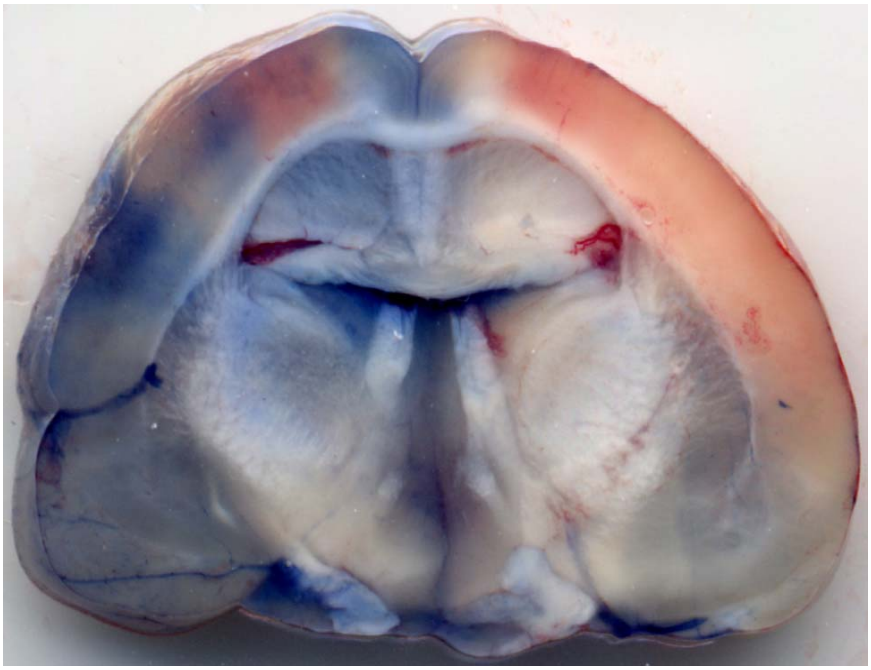

**Figure 7.1: Trypan Blue Demonstration of Hyperosmotic Mannitol Breakage of BBB**

**A demonstration of the expected distribution of a shift reagent in the rat brain after breakage of the BBB on the right side of the brain. Trypan blue, a histology dye that does not cross the BBB, was injected directly into the right CCA after a bolus injection of 25% w/v mannitol into the right CCA.**

Next, experiments were done to determine the rat's responses to the infusion of the SR (80mM $TmDOTP^{5-}$) and the bolus injection of the 25% w/v mannitol. Figure 7.2 shows a representative portion of the blood pressure (BP) trace for one of the $TmDOTP^{5-}$ infusion experiments. These experiments (n = 10 rats) demonstrated that infusion of the SR causes a decrease in the rat's BP, and that the slope of this BP decrease increases as the rate of the $TmDOTP^{5-}$ infusion is increased (rates tested were from 2.0-8.0mL/hr). The decrease in BP reverses when the SR infusion is stopped, as long as the BP is not too low at that point. (If the SR infusion is not stopped until the rat's BP (systolic) is below $30\pm5$ mmHg, then even after stopping the SR infusion the rat's BP usually does not recover, but instead it continues to decrease and the rat dies.) The decreasing of the rat's BP caused by the infusion of $TmDOTP^{5-}$ was found to lessen dramatically through simultaneous administration of 20mM $CaCl_2$ at 3.3mL/hr through a separate vessel cannulation (femoral vein). The bolus administration of 25% w/v mannitol into the CCA's causes an immediate drop in BP (although the BP returns to the pre-bolus level within 2 minutes). Depending on the mannitol bolus volume and whether it is given in one or both CCA's, the immediate drop in BP caused by the mannitol ranges from about 35-50 mmHg.

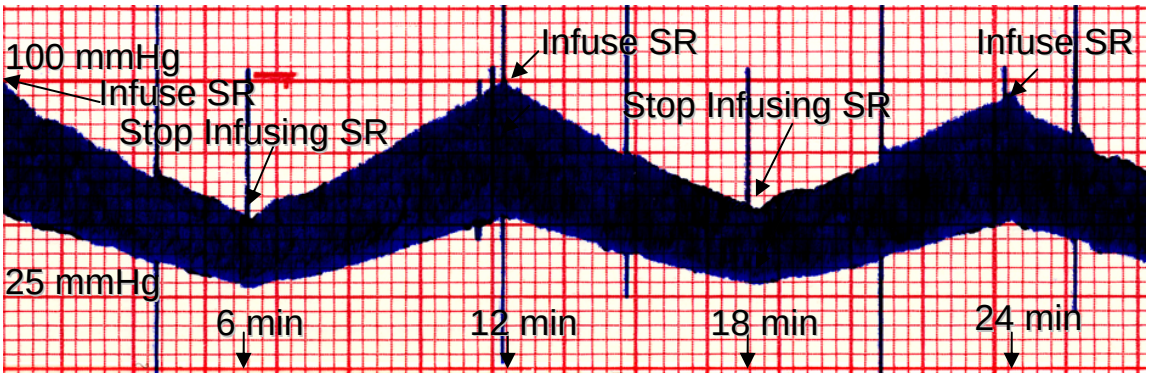


**Figure 7.2: BP Trace Showing Decrease in BP During SR Infusion Experiment in Rat**
**A representative portion of the BP trace for one of the SR infusion experiments. The BP (systolic arterial) is at 100 mmHg when the infusion of 80 mM TmDOTP5- is begun at a rate of 6.0 mL/hr. The infusion is stopped when the BP decreases to 50 mmHg (after about six minutes), the BP gradually increases back to the original value over the next six minutes, and then the infusion is started again. This cycle of staggered SR infusion is continued.**

Next, SQ sodium FID's were acquired on a saline phantom both before and after adding $TmDOTP^{5-}$. The SQ signal from the same amount of saline after $TmDOTP^{5-}$ was added to a concentration of 80mM was not only shifted in resonance frequency, but the SQ signal was also attenuated dramatically to less than 10% of the original signal intensity. Thus, the $TmDOTP^{5-}$ acts as both a shift reagent and an attenuation reagent.

Finally, the mannitol/$TmDOTP^{5-}$ sodium MR experiments were performed ($TmDOTP^{5-}$ bolus, n = 5 rats; $TmDOTP^{5-}$ infusion, n = 9 rats). Figure 7.3 shows the results from a $TmDOTP^{5-}$ bolus experiment. Figure 7.3 shows control SQ (top left) and control TQ (bottom left) spectra of the rat head before the administration of mannitol/$TmDOTP^{5-}$. In both of these spectra only a single resonance is visible, and it occurs at the center frequency, 0 kHz frequency

offset. Figure 7.3 also shows SR-aided SQ (top right) and SR-aided TQ (bottom right) spectra of the rat head after bolus injection of mannitol (3.8mL, 25% w/v) and then bolus injection of the SR (4.0mL of 80mM $TmDOTP^{5-}$) into both CCA's. Collected seven minutes after the SR injection, the SR-aided SQ spectrum (top right) demonstrates the shift in resonant frequency caused by the $TmDOTP^{5-}$. Two resonances are visible with a clear spread of resonant frequencies for the shifted peak (2-6 kHz frequency offset). The shifted resonance in this SR-aided SQ spectrum corresponds to signals from the extracellular space in the brain as well as the vascular and muscle extracellular spaces in the head. The SR-aided TQ spectrum (bottom right) has a peak at the center frequency, 0 kHz offset (i.e., the unshifted, intracellular sodium pool); however, there is no evidence of TQ signal from the extracellular sodium pool (i.e. at the 2-6 kHz frequency offset of the SR-shifted extracellular space).

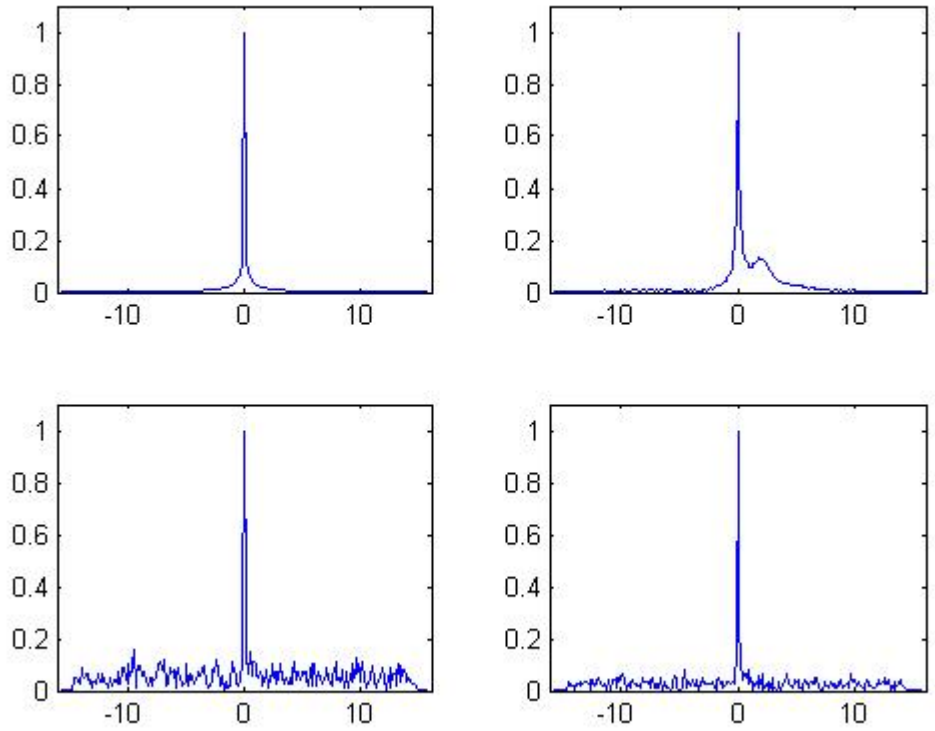


**Figure 7.3: Control and SR-Aided SQ and TQ NMR Spectra in SR Bolus Experiment**

**Control SQ (top left) and control TQ (bottom left) spectra of the rat head before the administration of mannitol/$TmDOTP^{5-}$, both showing a single resonance that occurs at the center frequency (0 kHz frequency offset). SR-aided SQ (top right) and SR-aided TQ (bottom right) spectra of rat head after bolus injection of mannitol followed by bolus injection of 80mM $TmDOTP^{5-}$ into both CCA's The SR-aided SQ spectrum demonstrates the presence of a shifted resonance with a clear spread of resonant frequencies for this shifted peak (2-6 kHz frequency offset), which corresponds to signals from the extracellular space in the brain as well as the vascular and muscle extracellular spaces in the head. The SR-aided TQ spectrum (bottom right) shows no evidence of any TQ signal from the extracellular sodium pool (i.e. at the 2-6 kHz frequency offset of the SR-shifted extracellular space).**

Figure 7.4 shows the results from a $TmDOTP^{5-}$ infusion experiment. Figure 4 shows control SQ (top left) and control TQ (bottom left) spectra of the rat head before the administration of mannitol/$TmDOTP^{5-}$. In both of these spectra only a single resonance is visible, and it occurs at the center frequency, 0 kHz frequency offset. Figure 7.4 also shows SR-aided SQ (top right) and SR-aided TQ (bottom right) spectra of the rat head after bolus injection of mannitol (3.8mL, 25% w/v) and then infusion of the SR (6.5mL of 80mM $TmDOTP^{5-}$) into both CCA's. The 80mM $TmDOTP^{5-}$ infusion was started at 4.0mL/hr and increased to 8.0mL/hr after 13 minutes. Two resonances are visible in the SR-aided SQ spectrum (top right) demonstrating the shift in resonant frequency caused by the $TmDOTP^{5-}$. The linewidth of the shifted peak in the SR-aided SQ spectra is smaller for the $TmDOTP^{5-}$ infusion experiment than for the $TmDOTP^{5-}$ bolus experiment. The SR-aided TQ spectrum (bottom right) has a peak at the center frequency, 0 kHz offset (i.e., the unshifted, intracellular sodium pool); however, again there is no evidence of TQ signal from the extracellular sodium pool (i.e. at the 2-6 kHz frequency offset of the SR-shifted extracellular space).

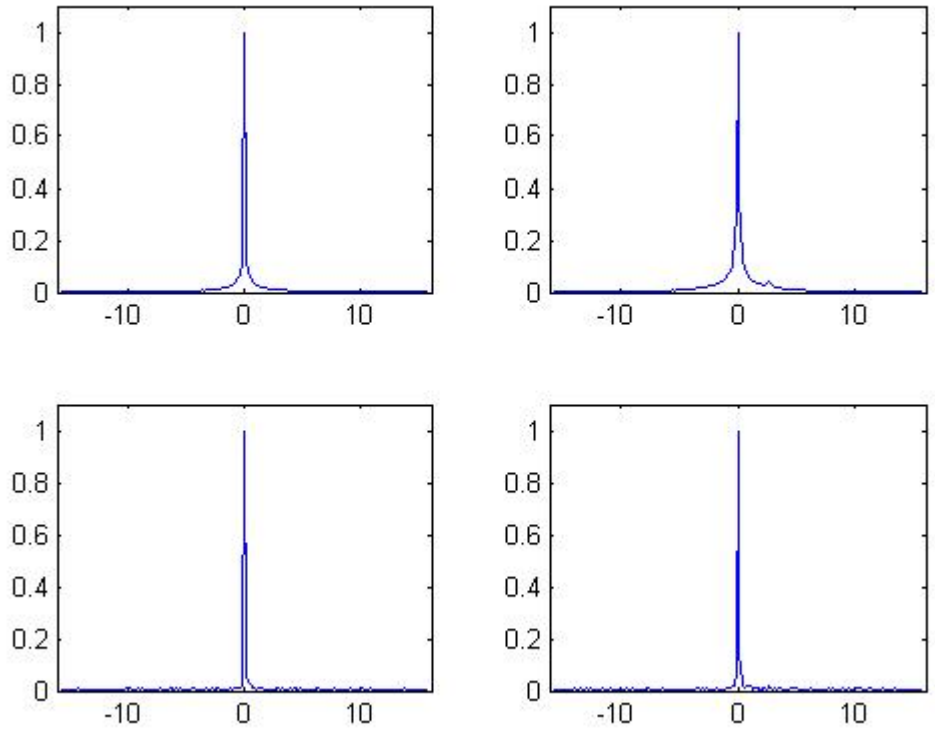


**Figure 7.4: Control and SR-Aided SQ and TQ NMR Spectra in SR Infusion Experiment**
**Control SQ (top left) and control TQ (bottom left) spectra of the rat head before the administration of mannitol/$TmDOTP^{5-}$, both showing a single resonance that occurs at the center frequency (0 kHz frequency offset). SR-aided SQ (top right) and SR-aided TQ (bottom right) spectra of rat head after bolus injection of mannitol followed by infusion of 80mM $TmDOTP^{5-}$ into both CCA's. Two resonances are visible in the SR-aided SQ spectrum demonstrating the shift in resonant frequency caused by the $TmDOTP^{5-}$. The shifted resonance corresponds to signals from the extracellular space in the brain as well as the vascular and muscle extracellular spaces in the head. The SR-aided TQ spectrum (bottom right) shows no evidence of any TQ signal from the extracellular sodium pool (i.e. at the 2-6 kHz frequency offset of the SR-shifted extracellular space).**

## 7.5 CONCLUSIONS

We have investigated the use of thulium ($TmDOTP^{5-}$) as a shift reagent in the *in vivo* rat brain. Our results indicate that the shift reagent can compromise the physiological status of the animal; however, separate administration of 20mM $CaCl_2$ through a separate vessel cannulation during $TmDOTP^{5-}$ administration allows maintenance of the animal's BP throughout the course of the experiment. As discussed previously, many NMR studies have shown that the TQ sodium MR signal is heavily weighted toward the intracellular sodium [14, 15, 25-30]. Our NMR results demonstrate that within the SNR of the experiment there is no evidence of any contribution to the TQ signal from the sodium in the extracellular brain, vascular, and muscle spaces in the head. This could be due to differences in transverse relaxation rates between the extracellular and intracellular compartments, and could be exacerbated by shift reagent-induced changes in the extracellular compartment. Nevertheless, our results indicate that the contribution from the extracellular sodium pool to the brain's TQ sodium MR signal is little to none. These results support the use of TQ sodium MRI for monitoring changes in the intracellular sodium concentration in evolving focal brain ischemia.

# 8.0 CONCLUSIONS

Stroke is the third leading cause of mortality in the United States and one of the major causes of serious, long-term disability among adults. In this thesis, sodium magnetic resonance has been implemented and investigated as an *in vivo* means for non-invasively visualizing the changes in cell sodium ion homeostasis that occur in ischemic tissue during acute stroke. There have been many reports in the literature studying the sodium ion accumulation that occurs in acute stroke using animal models of brain ischemia. However, most of these studies have used direct tissue analysis with flame photometry requiring a large number of animals at each time point. In addition, because each animal provided data at only a single time point, these studies did not allow the measurement of the tissue sodium concentration (TSC) for an individual animal over the entire time course of the stroke. Therefore, noninvasive techniques for the *in vivo* measurement of the sodium changes in acute stroke are highly desirable.

The introduction of thrombolytic therapy using tissue plasminogen activator (tPA) has revolutionized the treatment of acute stroke by providing an aggressive means for the reversal of the ischemic insult. At this time, the clinical decision as to whether to administer tPA therapy cannot be made based on the knowledge of the functional status of the ischemic brain tissue because there are no non-invasive means to quickly determine its viability. Instead, the time since the onset of symptoms is the current criterion for tPA administration. Because of the

sodium changes that occur in ischemic tissue during acute stroke, sodium MRI has the potential to extend the use of tPA to patients that would otherwise not receive treatment.

In this thesis, we hypothesized that the rate of tissue sodium concentration (TSC) increase can vary from patient to patient, and can also vary within the ischemic tissue of a single patient. To investigate this, we demonstrated the use of single quantum (SQ) sodium MRI for measuring the time course of TSC in a non-human primate model of reversible focal brain ischemia. In addition, a modification of the current "status quo" MAP2 immunostaining technique was developed to allow the histological verification of the brain infarct in this non-human primate model. The results of these studies indicate that TSC increases linearly in the ischemic tissue during arterial occlusion, that the rate of this TSC increase varies across the lesion, and that markedly different time courses of TSC ensue after restoration of blood flow. Our results demonstrate that the increase in TSC in ischemic tissue is readily measurable using sodium MRI at clinical magnetic field strengths (3.0 T) in acceptable imaging times (5 minutes). The results also indicate that sodium MRI could predict the stroke onset time in patients that are unsure when their symptoms began, potentially extending the use of tPA therapy to these patients. In addition, we believe that using sodium MRI to measure the rates of TSC increase across the ischemic tissue could help make the clinical decision regarding tPA administration based on whether a significant volume of tissue has only seen mild increases in TSC.

It has been hypothesized that the best means for the *in vivo* study of the changes in cell sodium ion homeostasis that occur during brain ischemia is to use schemes that isolate the sodium NMR signal from the intracellular compartment. Triple quantum (TQ) sodium NMR has been proposed as a scheme for this very purpose. To explore this, the contribution of the extracellular sodium pool to the brain's TQ sodium NMR signal was investigated in the rat using

the thulium shift reagent, $TmDOTP^{5-}$. The results demonstrated that within the SNR of the experiment there was no evidence of any contribution to the TQ signal from the sodium in the extracellular brain, vascular, and muscle spaces in the head. These results support TQ sodium NMR as a means to non-invasively isolate the sodium NMR signal from the intracellular sodium concentration.

Unfortunately, imaging extensions of these TQ techniques have been less common because of the weak nature of the TQ sodium NMR signal. Recently, though, our lab has developed efficient imaging schemes that allow the acquisition of TQ sodium MR images in clinically acceptable data acquisition times. In this thesis, TQ sodium MR images in the *in vivo* non-human primate are presented for the first time. Moreover, these images were obtained in clinically acceptable 18 minute data acquisition times. In these experiments, TQ sodium MR imaging was performed during non-human primate focal brain ischemia. TQ sodium MRI identified large changes in the ischemic region as early as 34 minutes after the onset of ischemia. The increase in the TQ sodium MRI signal intensity observed in the ischemic hemisphere is hypothesized to be due to an increase in the intracellular sodium concentration (ISC) as a result of impaired ion homeostasis during evolving brain ischemia.

In conclusion, our results support the hypothesis that developing the combination of SQ and TQ sodium MRI for non-invasively visualizing the changes in TSC and ISC across the ischemic lesion has the potential to significantly impact the clinical management of acute stroke. However, further experiments will be required to determine the level of the TSC threshold above which the tissue is no longer viable, and to elucidate whether the earlier identification of the ischemic lesion by TQ sodium MRI of ISC changes can also provide predictive information regarding tissue viability.

# APPENDIX

## TSC ERROR PROPAGATION ANALYSES AND LINEAR REGRESSION ANALYSES

Each SQ sodium MR image is 64 x 64 x 64 pixels. "Nuclear" magnetic resonance imaging is intrinsically quantitative, and therefore, the sodium MRI signal intensity for each pixel is proportional to the concentration of sodium nuclei present. The sodium MRI signal intensity for a specific pixel $(x, y, z)$ is given by

$$I(x,y,z) = C\rho(x,y,z)e^{-TE/T_2}\left(1-e^{-TR/T_1}\right)B_R(x,y,z)\sin\left(\gamma B_E(x,y,z)\Delta tA\right) \qquad \text{(A.1)}$$

where $C$ is a constant, $\rho(x,y,z)$ is the tissue sodium concentration, $TE$ is the echo time, $T_2$ is the effective transverse relaxation rate, $TR$ is the repetition time, $T_1$ is the longitudinal relaxation rate, $B_R(x,y,z)$ is the RF reception field, $\gamma$ is sodium's gyromagnetic ratio, $B_E(x,y,z)$ is the RF excitation field, $\Delta t$ is the RF pulse duration, and $A$ is the RF pulse amplitude. However, the twisted projection imaging (TPI) approach provides $TE << T_2$, so that $e^{-TE/T_2} \approx e^{-0} \approx 1$, and $TR$ is chosen so that $TR >> T_1$, so that $1-e^{-TR/T_1} \approx 1-e^{-\infty} \approx 1$. Therefore, Equation (A.1) becomes:

$$I(x,y,z) \approx C\rho(x,y,z)B_R(x,y,z)\sin\left(\gamma B_E(x,y,z)\Delta tA\right) \qquad \text{(A.2)}$$

In addition, the RF coil used is specifically designed so that the excitation and reception fields are nearly constant over the volume of interest (the animal's head), so that Equation (A.2) reduces to

$$I(x,y,z) \approx C\rho(x,y,z) \tag{A.3}$$

where the sodium MRI signal intensity $I(x,y,z)$ is proportional to the tissue sodium concentration $\rho(x,y,z)$. The proportionality constant $C$ for the conversion of the sodium MRI signal intensity to tissue sodium concentration (TSC) is determined using the sodium calibration standards within the image field of view.

The error in individual pixel TSC measurements was estimated for each SQ sodium MR image for each animal. This was done by measuring the standard deviation of the noise for that image and dividing by the mean contralateral brain signal intensity for that image. For the rest of the error propagation analysis, the highest resulting errors for each of the four animals will be used. The highest resulting error for individual pixel TSC measurements was 3.92% for animal #1, 2.65% for animal #2, 4.71% for animal #3, and 5.57% for animal #4. The error in the TSC measurement for a region of interest (ROI) decreases from these levels as the number of pixels within that ROI increases. If several SQ sodium MR images are acquired over time, a TSC slope map can be obtained, and the error in the individual TSC measurements can be propagated through to find the error in the resulting TSC slopes.

The TSC slope map is an image in which the intensity of each pixel represents the time rate of change of TSC (or the TSC slope) for that pixel. If $n$ is the number of SQ sodium MR images acquired over time for the calculation of the TSC slope map, then there are $n$ values of TSC over time for each of the 64 x 64 x 64 pixels. On a pixel by pixel basis, the TSC is plotted

versus time and a least squares linear regression is performed to determine the slope of the TSC increase, which is then tested for statistical significance.

Let $x_i$ for $i$ = 1 to $n$ be the times of the $n$ images. Then, for the specific pixel being investigated, let $y_i$ for $i$ = 1 to $n$ be the corresponding $n$ values of TSC (as % of normal). The mean of the $x_i$ values is $\overline{x} = \frac{1}{n}\sum_{i=1}^{n} x_i$ and the mean of the $y_i$ values is $\overline{y} = \frac{1}{n}\sum_{i=1}^{n} y_i$. The standard deviation of the $x_i$ values is $s_x = \sqrt{\frac{1}{n-1}\sum_{i=1}^{n}\left(x_i - \overline{x}\right)^2}$ and the standard deviation of the $y_i$ values is $s_y = \sqrt{\frac{1}{n-1}\sum_{i=1}^{n}\left(y_i - \overline{y}\right)^2}$.

The least squares linear regression analysis finds the best estimate for the TSC slope, $b$, and the best estimate for the y-intercept, $a$, for the best-fit line through the data given by the equation $\hat{y}_i = a + bx_i$. The best estimate for the TSC slope, $b$, is given by [67]:

$$b = \frac{\sum_{i=1}^{n}\left(x_i - \overline{x}\right)\left(y_i - \overline{y}\right)}{\sum_{i=1}^{n}\left(x_i - \overline{x}\right)^2} = \frac{n\sum_{i=1}^{n} x_i y_i - \sum_{i=1}^{n} x_i \sum_{i=1}^{n} y_i}{n\sum_{i=1}^{n} x_i^2 - \left(\sum_{i=1}^{n} x_i\right)^2} \tag{A.4}$$

The best estimate for the y-intercept, $a$, is then given by [67]:

$$a = \overline{y} - b\overline{x} = \frac{\sum_{i=1}^{n} y_i - b\sum_{i=1}^{n} x_i}{n} \tag{A.5}$$

Remember that the highest resulting error for individual pixel TSC measurements was $\Delta y_{max}$ = 3.92% for animal #1, $\Delta y_{max}$ = 2.65% for animal #2, $\Delta y_{max}$ = 4.71% for animal #3, and $\Delta y_{max}$ = 5.57% for animal #4. (Note that the image times, the $x_i$ values have no measurement error.) The $\Delta y_{max}$ error can be propagated through Equation (A.4) to find the measurement error

for the TSC slope $b$ for an individual pixel. The resulting error propagation equation for the TSC slope measurement error, $\Delta b_{\max}$, is

$$\Delta b_{\max} = \sqrt{\Delta y_{\max}^2 \left[ \sum_{i=1}^{n} \left( \frac{\partial b}{\partial y_i} \right)^2 \right]} \tag{A.6}$$

where the partial derivatives of $b$ with respect to the $y_i$ are given by

$$\frac{\partial b}{\partial y_i} = \frac{n x_i - \sum_{i=1}^{n} x_i}{n \sum_{i=1}^{n} x_i^2 - \left( \sum_{i=1}^{n} x_i \right)^2} \tag{A.7}$$

Using Equations (A.6) and (A.7) results in individual pixel TSC slope measurement errors of $\Delta b_{\max}$ = 1.04%/hr for animal #1 (where $n$ = 25), $\Delta b_{\max}$ = 1.06%/hr for animal #2 (where $n$ = 16), $\Delta b_{\max}$ = 1.83%/hr for animal #3 (where $n$ = 17), and $\Delta b_{\max}$ = 1.54%/hr for animal #4 (where $n$ = 24). These individual pixel TSC slope measurement errors $\Delta b_{\max}$ (as well as the even smaller ROI TSC slope measurement errors) were compared with the standard error in the slope of the linear regression $s_b$ (see below), and the larger of the two (which was always $s_b$) was the reported error in the TSC slope.

An analysis of variance procedure can then be performed in order to test the statistical significance of the slope of the linear regression [67]. The total sum of squares is given by:

$$\text{total } SS = \sum_{i=1}^{n} \left( y_i - \bar{y} \right)^2 = \sum_{i=1}^{n} y_i^2 - \frac{\left( \sum_{i=1}^{n} y_i \right)^2}{n} \tag{A.8}$$

The linear regression sum of squares is given by:

$$\text{regression } SS = \sum_{i=1}^{n}\left(\hat{y}_i - \bar{y}\right)^2 = b\left(\sum_{i=1}^{n} x_i y_i - \frac{1}{n}\sum_{i=1}^{n} x_i \sum_{i=1}^{n} y_i\right) = \frac{\left(\sum_{i=1}^{n} x_i y_i - \frac{1}{n}\sum_{i=1}^{n} x_i \sum_{i=1}^{n} y_i\right)^2}{\sum_{i=1}^{n} x_i^2 - \frac{1}{n}\left(\sum_{i=1}^{n} x_i\right)^2} \quad \text{(A.9)}$$

The coefficient of determination, $r^2$, is then given by:

$$r^2 = \frac{\text{regression } SS}{\text{total } SS} \quad \text{(A.10)}$$

The residual mean square, $s_{y\cdot x}^2$, is calculated as:

$$s_{y\cdot x}^2 = \frac{\text{total } SS - \text{regression } SS}{n-2} = s_y^2\left(1-r^2\right)\left(\frac{n-1}{n-2}\right) \quad \text{(A.11)}$$

The standard error of the slope of the linear regression, $s_b$, can then be calculated as [67]:

$$s_b = \sqrt{\frac{s_{y\cdot x}^2}{\sum_{i=1}^{n}\left(x_i - \bar{x}\right)^2}} = \sqrt{\frac{s_{y\cdot x}^2}{\sum_{i=1}^{n} x_i^2 - \frac{1}{n}\left(\sum_{i=1}^{n} x_i\right)^2}} \quad \text{(A.12)}$$

A two-tailed student's t-test can then be used to test for the statistical significance of the linear regression results for the TSC slope, $b$, for the pixel being investigated. The t-statistic for testing the null hypothesis, $H_0$: the TSC slope = 0, versus the alternate hypothesis, $H_A$: the TSC slope ≠ 0, is given by:

$$t = \frac{b-0}{s_b} \quad \text{(A.13)}$$

A 5% significance level for the two-tailed t-test is used, and the degrees of freedom for this testing procedure are $n-2$. Finally, if the calculated t-statistic, $t = \frac{b-0}{s_b}$, is greater than the critical value of $t_{0.05(2),n-2}$ then the TSC slope, $b$, for that pixel is statistically significant with

$p < 0.05$, and it is included in the resulting TSC slope map. This same procedure is then performed for each of the 64 x 64 x 64 pixels.

As an example of calculating the t-statistic and comparing it to the critical value of $t_{0.05(2),n-2}$, this same procedure for testing the statistical significance was used for the ROI TSC slope determined from the linear regression of the data shown graphically for animal #2 in Figure 5.4. The linear regression of the TSC values from the $n = 16$ images over time resulted in a TSC slope calculated from Equation (A.4) of $b = 7.15\%$/hr. Next, using Equation (A.12), the standard error of $b$ was determined to be $s_b = 0.682\%$/hr (compared to $\Delta b_{\max} = 0.142\%$/hr for this ROI). Then, the t-statistic was calculated using Equation (A.13) to be $t = 10.5$. Using the degrees of freedom of $n - 2 = 14$, the critical value is $t_{0.05(2),n-2} = t_{0.05(2),14} = 2.145$. Therefore, because the t-statistic of $t = 10.5$ is greater than the critical value of $t_{0.05(2),14} = 2.145$, then the TSC slope of $b = 7.15\%$/hr is statistically significant with $p < 0.05$. Finally, $b \pm s_b t_{0.05(2),n-2}$ provides a 95% confidence interval for the TSC slope, which in this case is $b \pm s_b t_{0.05(2),14} = 7.15 \pm 1.46\%$/hr.

## BIBLIOGRAPHY


1. Liang Z, Lauterbur PC. Principles of Magnetic Resonance Imaging: A Signal Processing Perspective. 2000, Piscataway, NJ: IEEE Press.

2. Young SW. Nuclear Magnetic Resonance Imaging. 1984, New York: Raven Press.

3. Lauterbur PC. Image formation by induced local interactions: Examples employing nuclear magnetic resonance. Nature 1973; **242**: 190-191.

4. Sigal R, Doyon D, Halimi Ph, Atlan H. Magnetic Resonance Imaging. 1988, Berlin: Springer-Verlag.

5. Lufkin RB. The MRI Manual. 1990, Chicago: Year Book Medical Publishers.

6. Horowitz AL. MRI Physics for Radiologists: A Visual Approach. 1995, New York: Springer-Verlag.

7. Morris PG. Nuclear Magnetic Resonance Imaging in Medicine and Biology. 1986, New York: Oxford University Press.

8. Young SW. Magnetic Resonance Imaging: Basic Principles, 2nd ed. 1988, New York: Raven Press.

9. Mitchell DG, Cohen MS. MRI Principles, 2nd ed. 2004, Philadelphia: Saunders Publishing.

10. Tipler PA. Physics for Scientists and Engineers, 3rd ed. 1991, New York: Worth Publishers.

11. Partain CL, James AE, Rollo FD, Price RR. Nuclear Magnetic Resonance (NMR) Imaging. 1983, Philadelphia: W. B. Saunders Company.

12. Fukushima E, Roeder SBW. Experimental Pulse NMR: A Nuts and Bolts Approach. 1981, Reading, MA: Addison-Wesley Publishing Company.

13. Kaufman L, Crooks LE, Margulis AR. Nuclear Magnetic Resonance Imaging in Medicine. 1981, New York: Igaku-Shoin Medical Publishers.

14. Seshan V, Germann MJ, Preisig P, Malloy CR, Sherry AD, Bansal N. $TmDOTP^{5-}$ as a $^{23}Na$ shift reagent for the in vivo rat kidney. Magn Reson Med 1995; 34(1): 25-31.

15. Seshan V, Sherry AD, Bansal N. Evaluation of triple quantum-filtered $^{23}Na$ NMR spectroscopy in the in situ rat liver. Magn Reson Med 1997; 38(5): 821-827.

16. Hancu I, Boada FE, Shen GX. Three-dimensional triple-quantum-filtered $^{23}Na$ imaging of in vivo human brain. Magn Reson Med 1999; 42(6): 1146-1154.

17. Edelstein WA, Hutchison JM, Johnson G, Redpath T. Spin warp NMR imaging and applications to human whole-body imaging. Phys Med Biol 1980; 25(4): 751-756.

18. Boada FE, Christensen JD, Huang-Hellinger FR, Reese TG, Thulborn KR. Quantitative in vivo tissue sodium concentration maps: the effects of biexponential relaxation. Magn Reson Med 1994; 32(2): 219-223.

19. Boada FE, Gillen JS, Shen GX, Chang SY, Thulborn KR. Fast three dimensional sodium imaging. Magn Reson Med 1997; 37(5): 706-715.

20. Constantinides CD, Kraitchman DL, O'Brien KO, Boada FE, Gillen J, Bottomley PA. Noninvasive quantification of total sodium concentrations in acute reperfused myocardial infarction using $^{23}Na$ MRI. Magn Reson Med 2001; 46(6): 1144-1151.

21. Constantinides CD, Gillen JS, Boada FE, Pomper MG, Bottomley PA. Human skeletal muscle: Sodium MR imaging and quantification – potential applications in exercise and disease. Radiology 2000; 216(2): 559-568.

22. Christensen JD, Barrere BJ, Boada FE, Vevea JM, Thulborn KR. Quantitative tissue sodium concentration mapping of normal rat brain. Magn Reson Med 1996; 36(1): 83-89.

23. Boada FE, LaVerde G, Jungreis C, Nemoto E, Tanase C, and Hancu I. Loss of cell ion homeostasis and cell viability in the brain: What sodium MRI can tell us. In: In vivo Cellular and Molecular Imaging. Ahrens ET, editor. Philadelphia, Academic Press. Current Topics in Developmental Biology 2005; 70: 77-101.

24. Hancu I, van der Maarel JRC, Boada FE. A model for the dynamics of spins 3/2 in biological media: signal loss during radiofrequency excitation in triple-quantum-filtered sodium MRI. J Magn Reson 2000; 147(2): 179-191.

25. Navon G. Complete elimination of the extracellular 23Na NMR signal in triple quantum filtered spectra of rat hearts in the presence of shift reagents. Magn Reson Med 1993; 30: 503-506.

26. Hutchinson R, Huntley JJA, Zhou HZ, Ciesla DJ, Shapiron JI. Changes in double quantum filtered sodium intensity during prolonged ischemia in the isolated perfused heart. Magn Reson Med 1993; 29: 391-395.

27. Lyon R, Pekar J, Moonen C, Mclaughlin A. Double-quantum surface-coil NMR studies of sodium and potassium in the rat brain. Magn Reson Med 1991; 18: 80-92.

28. Tauskela JS, Dizpn JM, Whang J, Katz J. Evaluation of multiple-quantum-filtered 23Na NMR in monitoring intracellular Na content in the isolated perfused rat heart in the absence of a chemical shift reagent. J Magn Reson 1997; 127: 115-127.

29. Knubovets T, Shinar H, Navon G. Quantification of the contribution of extracellular sodium to Na-23 multiple-quantum-filtered NMR spectra of suspensions of human red blood cells. J Magn Reson 1998; 131: 92-96.

30. LaVerde GC, Tanase C, Boada FE. Contribution of the Extracellular Sodium Pool to the Brain's Triple Quantum Sodium MR Signal. In: Proceedings of the 13th Annual Meeting of ISMRM, Miami Beach, FL, USA, 2005; p. 2483.

31. Kalyanapuram R, Seshan V, Bansal N. Three-dimensional triple-quantum-filtered $^{23}$Na imaging of the dog head in vivo. J Magn Reson Imag 1998; 8: 1182-1189.

32. The National Institute of Neurological Disorders and Stroke rt-PA Stroke Study Group. Tissue plasminogen activator for acute ischemic stroke. New England Journal of Medicine 1995; 333(24): 1581-1587.

33. Kidwell CS, Saver JL, Mattiello J, Starkman S, Vinuela F, Duckwiler G, Gobin YP, Jahan R, Vespa P, Kalafut M, Alger JR. Thrombolytic reversal of acute human cerebral ischemic injury shown by diffusion/perfusion magnetic resonance imaging. Annals of Neurology 2000; 47(4): 462-469.

34. Ito U, Ohno K, Nakamura R, Suganuma F, Inaba Y. Brain edema during ischemia and after restoration of blood flow. Stroke 1979; 10(5): 542-547.

35. Wang Y, Hu W, Perez-Trepichio AD, Ng TC, Furlan AJ, Majors AW, Jones SC. Brain tissue sodium is a ticking clock telling time after arterial occlusion in rat focal cerebral ischemia. Stroke 2000; 31(6): 1386-1391.

36. Young W, Rappaport Z, Chalif D, Flamm E. Regional brain sodium, potassium, and water changes in the rat middle cerebral artery occlusion model of ischemia. Stroke 1987; 18: 751-759.

37. Dickinson LD, Betz AL. Attenuated development of ischemic brain edema in vasopressin-deficient rats. J Cereb Blood Flow Metab 1992; 12: 681-690.

38. Schuier FJ, Hossman KA. Experimental brain infarcts in cats, II: Ischemic brain edema. Stroke 1980; 11: 593-601.

39. Lo WD, Betz AL, Schielke GP, Hoff JT. Transport of sodium from blood to brain in ischemic brain edema. Stroke 1987; 18: 150-157.

40. Betz AL, Keep RF, Beer ME, Ren XD. Blood-brain barrier permeability and brain concentration of sodium, potassium, and chloride during focal ischemia. J Cereb Blood Flow Metab 1994; 14(1): 29-37.

41. Jones SC, Kharlamov A, Yanovski B, Kim DK, Easley KA, Yushmanov VE, Ziolko SK, Boada FE. Stroke onset time using sodium MRI in rat focal cerebral ischemia. Stroke 2006; 37(3): 883-888.

42. Thulborn KR, Gindin TS, Davis D, Erb P. Comprehensive MRI protocol for stroke management: Tissue sodium concentration as a measure of tissue viability in non-human primate studies and in clinical studies. Radiology 1999; 213: 156-166.

43. Memezawa H, Smith ML, Siesjo BK. Penumbral tissues salvaged by reperfusion following middle cerebral artery occlusion in rats. Stroke 1992; 23(4): 552-559.

44. Kaplan B, Brint S, Tanabe J, Jacewicz M, Wang XJ, Pulsinelli W. Temporal thresholds for neocortical infarction in rats subjected to reversible focal cerebral ischemia. Stroke 1991; 22(8): 1032-1039.

45. Marcoux FW, Morawetz RB, Crowell RM, DeGirolami U, Halsey JH Jr. Differential regional vulnerability in transient focal cerebral ischemia. Stroke 1982; 13(3): 339-346.

46. Jones TH, Morawetz RB, Crowell RM, Marcoux FW, FitzGibbon SJ, DeGirolami U, Ojemann RG. Thresholds of focal cerebral ischemia in awake monkeys. J Neurosurg 1981; 54(6): 773-782.

47. Jungreis CA, Nemoto E, Boada F, Horowitz MB. Model of Reversible Cerebral Ischemia in a Monkey Model. Am J Neuroradiology 2003; 24: 1834-1836.

48. Isayama K, Pitts LH, Nishimura MC. Evaluation of 2,3,5-triphenyltetrazolium chloride staining to delineate rat brain infarcts. Stroke 1991; 22(11): 1394-1398.

49. Bederson JB, Pitts LH, Germano SM, Nishimura MC, Davis RL, Bartkowski HM. Evaluation of 2,3,5-triphenyltetrazolium chloride as a stain for detection and quantification of experimental cerebral infarction in rats. Stroke 1986; 17: 1304-1308.

50. Hatfield RH, Mendelow AD, Perry RH, Alvarez LM, Modha P. Triphenyltetrazolium chloride (TTC) as a marker for ischaemic changes in rat brain following permanent middle cerebral artery occlusion. Neuropathol Appl Neurobiol 1991; 17(1): 61-67.

51. Bednar MM, Fanburg JC, Anderson ML, Raymond SJ, Dooley RH, Gross CE. Comparison of triphenyltetrazolium dye with light microscopic evaluation in a rabbit model of acute cerebral ischaemia. Neurol Res 1994; 16(2): 129-132.

52. Dawson DA, Hallenbeck JM. Acute focal ischemia-induced alterations in MAP2 immunostaining: Description of temporal changes and utilization as a marker for volumetric assessment of acute brain injury. J Cereb Blood Flow Metab 1996; 16:170-4.

53. Kharlamov A, Jones SC, Kim DK. Suramin reduces infarct volume in a model of focal brain ischemia in rats. Exp Brain Res 2002; 147: 353-359.

54. Kharlamov A, Kim DK, Jones SC. Early visual changes in reflected light on non-stained brain sections after focal ischemia mirror the area of ischemic damage. J Neurosci Meth 2001; 111: 67-73.

55. Yanagihara T, Brengman JM, Mushynski WE. Differential vulnerability of microtubule components in cerebral ischemia. Acta Neuropathol (Berl) 1990; 80: 499-505.

56. Miyazawa T, Bonnekoh P, Hossmann KA. Temperature effect on immunostaining of microtubule-associated protein 2 and synaptophysin after 30 minutes of forebrain ischemia in rat. Acta Neuropathol (Berl) 1993; 85: 526-532.

57. Pettigrew LC, Holtz ML, Craddock SD, Minger SL, Hall N, Geddes JW. Microtubular proteolysis in focal cerebral ischemia. J Cereb Blood Flow Metab 1996; 16: 1189-1202.

58. Koizumi J, Yoshida Y, Nakazawa T, Ooneda G. Experimental studies of ischemic brain edema. 1. A new experimental model of cerebral embolism in rats in which recirculation can be introduced in the ischemic area. Jpn J Stroke 1986; 8: 1-8.

59. Nagasawa H, Kogure K. Correlation between cerebral blood flow and histologic changes in a new rat model of middle cerebral artery occlusion. Stroke 1989; 20(8): 1037-1043.

60. Hsu SM, Raine L. Protein A, avidin, and biotin in immunohistochemistry. J Histochem Cytochem 1981; 29: 1349-1353.

61. Loening AM, Gambhir SS. AMIDE: A Free Software Tool for Multimodality Medical Image Analysis. Molecular Imag 2003; 2(3): 131-137.

62. Rorden, C., Brett, M. Stereotaxic display of brain lesions. Behavioural Neurology 2000; 12: 191-200.

63. Bhattacharjee AK, Nagashima T, Kondoh T, and Tamaki N. Quantification of early blood-brain barrier disruption by in situ brain perfusion technique. Brain Research Protocols 2001; 8: 126-131.

64. Ikeda M, Bhattacharjee AK, Kondoh T, Nagashima T, and Tamaki N. Synergistic effect of cold mannitol and $Na^{+}/Ca^{2+}$ exchange blocker on blood-brain barrier opening. Biochemical and Biophysical Research Communications 2002; 291: 669-674.

65. Shen GX, Boada FE, Thulborn KR. Dual-frequency, dual-quadrature, birdcage RF coil design with identical B1 pattern for sodium and proton imaging of the human brain at 1.5 T. Magnetic Resonance in Medicine 1997; 38(5): 717-725.

66. Granholm ACE, Curtis M, Diamond DM, Branch BJ, Heman KL, Rose GM. Development of an intact blood-brain barrier in brain tissue transplants is dependent on the site of transplantation. Cell Transplantation 1996; 5: 305-314.

67. Zar JH. Biostatistical Analysis, 4th ed. 1999, Upper Saddle River, NJ: Prentice-Hall.